Evidence for CP violation in $B^+ \to K^*(892)^+\pi^0$ from a Dalitz plot analysis of $B^+ \to K^0_S\pi^+\pi^0$ decays

J. P. Lees,[1] V. Poireau,[1] V. Tisserand,[1] E. Grauges,[2] A. Palano,[3a,3b] G. Eigen,[4] B. Stugu,[4] D. N. Brown,[5] L. T. Kerth,[5] Yu. G. Kolomensky,[5] M. J. Lee,[5] G. Lynch,[5] H. Koch,[6] T. Schroeder,[6] C. Hearty,[7] T. S. Mattison,[7] J. A. McKenna,[7] R. Y. So,[7] A. Khan,[8] V. E. Blinov,[9a,9b,9c] A. R. Buzykaev,[9a] V. P. Druzhinin,[9a,9b] V. B. Golubev,[9a,9b] E. A. Kravchenko,[9a,9b] A. P. Onuchin,[9a,9b,9c] S. I. Serednyakov,[9a,9b] Yu. I. Skovpen,[9a,9b] E. P. Solodov,[9a,9b] K. Yu. Todyshev,[9a,9b] A. J. Lankford,[10] B. Dey,[11] J. W. Gary,[11] O. Long,[11] M. Franco Sevilla,[12] T. M. Hong,[12] D. Kovalskyi,[12] J. D. Richman,[12] C. A. West,[12] A. M. Eisner,[13] W. S. Lockman,[13] W. Panduro Vazquez,[13] B. A. Schumm,[13] A. Seiden,[13] D. S. Chao,[14] C. H. Cheng,[14] B. Echenard,[14] K. T. Flood,[14] D. G. Hitlin,[14] T. S. Miyashita,[14] P. Ongmongkolkul,[14] F. C. Porter,[14] M. Röhrken,[14] R. Andreassen,[15] Z. Huard,[15] B. T. Meadows,[15] B. G. Pushpawela,[15] M. D. Sokoloff,[15] L. Sun,[15] P. C. Bloom,[16] W. T. Ford,[16] A. Gaz,[16] J. G. Smith,[16] S. R. Wagner,[16] R. Ayad,[17,†] W. H. Toki,[17] B. Spaan,[18] D. Bernard,[19] M. Verderi,[19] S. Playfer,[20] D. Bettoni,[21a] C. Bozzi,[21a] R. Calabrese,[21a,21b] G. Cibinetto,[21a,21b] E. Fioravanti,[21a,21b] I. Garzia,[21a,21b] E. Luppi,[21a,21b] L. Piemontese,[21a] V. Santoro,[21a] A. Calcaterra,[22] R. de Sangro,[22] G. Finocchiaro,[22] S. Martellotti,[22] P. Patteri,[22] I. M. Peruzzi,[22,‡] M. Piccolo,[22] M. Rama,[22] A. Zallo,[22] R. Contri,[23a,23b] M. R. Monge,[23a,23b] S. Passaggio,[23a] C. Patrignani,[23a,23b] B. Bhuyan,[24] V. Prasad,[24] A. Adametz,[25] U. Uwer,[25] H. M. Lacker,[26] U. Mallik,[27] C. Chen,[28] J. Cochran,[28] S. Prell,[28] H. Ahmed,[29] A. V. Gritsan,[30] N. Arnaud,[31] M. Davier,[31] D. Derkach,[31] G. Grosdidier,[31] F. Le Diberder,[31] A. M. Lutz,[31] B. Malaescu,[31,§] P. Roudeau,[31] A. Stocchi,[31] G. Wormser,[31] D. J. Lange,[32] D. M. Wright,[32] J. P. Coleman,[33] J. R. Fry,[33] E. Gabathuler,[33] D. E. Hutchcroft,[33] D. J. Payne,[33] C. Touramanis,[33] A. J. Bevan,[34] F. Di Lodovico,[34] R. Sacco,[34] G. Cowan,[35] D. N. Brown,[36] C. L. Davis,[36] A. G. Denig,[37] M. Fritsch,[37] W. Gradl,[37] K. Griessinger,[37] A. Hafner,[37] K. R. Schubert,[37] R. J. Barlow,[38,‖] G. D. Lafferty,[38] R. Cenci,[39] B. Hamilton,[39] A. Jawahery,[39] D. A. Roberts,[39] R. Cowan,[40] R. Cheaib,[41] P. M. Patel,[41,*] S. H. Robertson,[41] N. Neri,[42a] F. Palombo,[42a,42b] L. Cremaldi,[43] R. Godang,[43,¶] D. J. Summers,[43] M. Simard,[44] P. Taras,[44] G. De Nardo,[45a,45b] G. Onorato,[45a,45b] C. Sciacca,[45a,45b] G. Raven,[46] C. P. Jessop,[47] J. M. LoSecco,[47] K. Honscheid,[48] R. Kass,[48] M. Margoni,[49a,49b] M. Morandin,[49a] M. Posocco,[49a] M. Rotondo,[49a] G. Simi,[49a,49b] F. Simonetto,[49a,49b] R. Stroili,[49a,49b] S. Akar,[50] E. Ben-Haim,[50] M. Bomben,[50] G. R. Bonneaud,[50] H. Briand,[50] G. Calderini,[50] J. Chauveau,[50] Ph. Leruste,[50] G. Marchiori,[50] J. Ocariz,[50] M. Biasini,[51a,51b] E. Manoni,[51a] A. Rossi,[51a] C. Angelini,[52a,52b] G. Batignani,[52a,52b] S. Bettarini,[52a,52b] M. Carpinelli,[52a,52b,**] G. Casarosa,[52a,52b] M. Chrzaszcz,[52a] F. Forti,[52a,52b] M. A. Giorgi,[52a,52b] A. Lusiani,[52a,52c] B. Oberhof,[52a,52b] E. Paoloni,[52a,52b] G. Rizzo,[52a,52b] J. J. Walsh,[52a] D. Lopes Pegna,[53] J. Olsen,[53] A. J. S. Smith,[53] F. Anulli,[54a] R. Faccini,[54a,54b] F. Ferrarotto,[54a] F. Ferroni,[54a,54b] M. Gaspero,[54a,54b] A. Pilloni,[54a,54b] G. Piredda,[54a] C. Bünger,[55] S. Dittrich,[55] O. Grünberg,[55] M. Hess,[55] T. Leddig,[55] C. Voß,[55] R. Waldi,[55] T. Adye,[56] E. O. Olaiya,[56] F. F. Wilson,[56] S. Emery,[57] G. Vasseur,[57] D. Aston,[58] D. J. Bard,[58] C. Cartaro,[58] M. R. Convery,[58] J. Dorfan,[58] G. P. Dubois-Felsmann,[58] W. Dunwoodie,[58] M. Ebert,[58] R. C. Field,[58] B. G. Fulsom,[58] M. T. Graham,[58] C. Hast,[58] W. R. Innes,[58] P. Kim,[58] D. W. G. S. Leith,[58] D. Lindemann,[58] S. Luitz,[58] V. Luth,[58] H. L. Lynch,[58] D. B. MacFarlane,[58] D. R. Muller,[58] H. Neal,[58] M. Perl,[58,*] T. Pulliam,[58] B. N. Ratcliff,[58] A. Roodman,[58] R. H. Schindler,[58] A. Snyder,[58] D. Su,[58] M. K. Sullivan,[58] J. Va'vra,[58] W. J. Wisniewski,[58] H. W. Wulsin,[58] M. V. Purohit,[59] J. R. Wilson,[59] A. Randle-Conde,[60] S. J. Sekula,[60] M. Bellis,[61] P. R. Burchat,[61] E. M. T. Puccio,[61] M. S. Alam,[62] J. A. Ernst,[62] R. Gorodeisky,[63] N. Guttman,[63] D. R. Peimer,[63] A. Soffer,[63] S. M. Spanier,[64] J. L. Ritchie,[65] R. F. Schwitters,[65] J. M. Izen,[66] X. C. Lou,[66] F. Bianchi,[67a,67b] F. De Mori,[67a,67b] A. Filippi,[67a] D. Gamba,[67a,67b] L. Lanceri,[68a,68b] L. Vitale,[68a,68b] F. Martinez-Vidal,[69] A. Oyanguren,[69] P. Villanueva-Perez,[69] J. Albert,[70] Sw. Banerjee,[70] A. Beaulieu,[70] F. U. Bernlochner,[70] H. H. F. Choi,[70] G. J. King,[70] R. Kowalewski,[70] M. J. Lewczuk,[70] T. Lueck,[70] I. M. Nugent,[70] J. M. Roney,[70] R. J. Sobie,[70] N. Tasneem,[70] T. J. Gershon,[71] P. F. Harrison,[71] T. E. Latham,[71] H. R. Band,[72] S. Dasu,[72] Y. Pan,[72] R. Prepost,[72] and S. L. Wu[72]

(The *BABAR* Collaboration)

[1]*Laboratoire d'Annecy-le-Vieux de Physique des Particules (LAPP), Université de Savoie, CNRS/IN2P3, F-74941 Annecy-Le-Vieux, France*
[2]*Universitat de Barcelona, Facultat de Fisica, Departament ECM, E-08028 Barcelona, Spain*
[3a]*INFN Sezione di Bari, I-70126 Bari, Italy*
[3b]*Dipartimento di Fisica, Università di Bari, I-70126 Bari, Italy*
[4]*University of Bergen, Institute of Physics, N-5007 Bergen, Norway*
[5]*Lawrence Berkeley National Laboratory and University of California, Berkeley, California 94720, USA*
[6]*Ruhr Universität Bochum, Institut für Experimentalphysik 1, D-44780 Bochum, Germany*
[7]*University of British Columbia, Vancouver, British Columbia, Canada V6T 1Z1*
[8]*Brunel University, Uxbridge, Middlesex UB8 3PH, United Kingdom*

[9a]*Budker Institute of Nuclear Physics SB RAS, Novosibirsk 630090, Russia*
[9b]*Novosibirsk State University, Novosibirsk 630090, Russia*
[9c]*Novosibirsk State Technical University, Novosibirsk 630092, Russia*
[10]*University of California at Irvine, Irvine, California 92697, USA*
[11]*University of California at Riverside, Riverside, California 92521, USA*
[12]*University of California at Santa Barbara, Santa Barbara, California 93106, USA*
[13]*University of California at Santa Cruz, Institute for Particle Physics, Santa Cruz, California 95064, USA*
[14]*California Institute of Technology, Pasadena, California 91125, USA*
[15]*University of Cincinnati, Cincinnati, Ohio 45221, USA*
[16]*University of Colorado, Boulder, Colorado 80309, USA*
[17]*Colorado State University, Fort Collins, Colorado 80523, USA*
[18]*Technische Universität Dortmund, Fakultät Physik, D-44221 Dortmund, Germany*
[19]*Laboratoire Leprince-Ringuet, Ecole Polytechnique, CNRS/IN2P3, F-91128 Palaiseau, France*
[20]*University of Edinburgh, Edinburgh EH9 3JZ, United Kingdom*
[21a]*INFN Sezione di Ferrara, I-44122 Ferrara, Italy*
[21b]*Dipartimento di Fisica e Scienze della Terra, Università di Ferrara, I-44122 Ferrara, Italy*
[22]*INFN Laboratori Nazionali di Frascati, I-00044 Frascati, Italy*
[23a]*INFN Sezione di Genova, I-16146 Genova, Italy*
[23b]*Dipartimento di Fisica, Università di Genova, I-16146 Genova, Italy*
[24]*Indian Institute of Technology Guwahati, Guwahati, Assam 781 039, India*
[25]*Universität Heidelberg, Physikalisches Institut, D-69120 Heidelberg, Germany*
[26]*Humboldt-Universität zu Berlin, Institut für Physik, D-12489 Berlin, Germany*
[27]*University of Iowa, Iowa City, Iowa 52242, USA*
[28]*Iowa State University, Ames, Iowa 50011-3160, USA*
[29]*Physics Department, Jazan University, Jazan 22822, Kingdom of Saudia Arabia*
[30]*Johns Hopkins University, Baltimore, Maryland 21218, USA*
[31]*Laboratoire de l'Accélérateur Linéaire, IN2P3/CNRS et Université Paris-Sud 11, Centre Scientifique d'Orsay, F-91898 Orsay Cedex, France*
[32]*Lawrence Livermore National Laboratory, Livermore, California 94550, USA*
[33]*University of Liverpool, Liverpool L69 7ZE, United Kingdom*
[34]*Queen Mary, University of London, London E1 4NS, United Kingdom*
[35]*University of London, Royal Holloway and Bedford New College, Egham, Surrey TW20 0EX, United Kingdom*
[36]*University of Louisville, Louisville, Kentucky 40292, USA*
[37]*Johannes Gutenberg-Universität Mainz, Institut für Kernphysik, D-55099 Mainz, Germany*
[38]*University of Manchester, Manchester M13 9PL, United Kingdom*
[39]*University of Maryland, College Park, Maryland 20742, USA*
[40]*Massachusetts Institute of Technology, Laboratory for Nuclear Science, Cambridge, Massachusetts 02139, USA*
[41]*McGill University, Montréal, Québec, Canada H3A 2T8*
[42a]*INFN Sezione di Milano, I-20133 Milano, Italy*
[42b]*Dipartimento di Fisica, Università di Milano, I-20133 Milano, Italy*
[43]*University of Mississippi, University, Mississippi 38677, USA*
[44]*Université de Montréal, Physique des Particules, Montréal, Québec, Canada H3C 3J7*
[45a]*INFN Sezione di Napoli, I-80126 Napoli, Italy*
[45b]*Dipartimento di Scienze Fisiche, Università di Napoli Federico II, I-80126 Napoli, Italy*
[46]*NIKHEF, National Institute for Nuclear Physics and High Energy Physics, NL-1009 DB Amsterdam, The Netherlands*
[47]*University of Notre Dame, Notre Dame, Indiana 46556, USA*
[48]*Ohio State University, Columbus, Ohio 43210, USA*
[49a]*INFN Sezione di Padova, I-35131 Padova, Italy*
[49b]*Dipartimento di Fisica, Università di Padova, I-35131 Padova, Italy*
[50]*Laboratoire de Physique Nucléaire et de Hautes Energies, IN2P3/CNRS, Université Pierre et Marie Curie-Paris6, Université Denis Diderot-Paris7, F-75252 Paris, France*
[51a]*INFN Sezione di Perugia, I-06123 Perugia, Italy*
[51b]*Dipartimento di Fisica, Università di Perugia, I-06123 Perugia, Italy*
[52a]*INFN Sezione di Pisa, I-56127 Pisa, Italy*
[52b]*Dipartimento di Fisica, Università di Pisa, I-56127 Pisa, Italy*
[52c]*Scuola Normale Superiore di Pisa, I-56127 Pisa, Italy*
[53]*Princeton University, Princeton, New Jersey 08544, USA*

[54a]*INFN Sezione di Roma, I-00185 Roma, Italy*
[54b]*Dipartimento di Fisica, Università di Roma La Sapienza, I-00185 Roma, Italy*
[55]*Universität Rostock, D-18051 Rostock, Germany*
[56]*Rutherford Appleton Laboratory, Chilton, Didcot, Oxon OX11 0QX, United Kingdom*
[57]*CEA, Irfu, SPP, Centre de Saclay, F-91191 Gif-sur-Yvette, France*
[58]*SLAC National Accelerator Laboratory, Stanford, California 94309 USA*
[59]*University of South Carolina, Columbia, South Carolina 29208, USA*
[60]*Southern Methodist University, Dallas, Texas 75275, USA*
[61]*Stanford University, Stanford, California 94305-4060, USA*
[62]*State University of New York, Albany, New York 12222, USA*
[63]*Tel Aviv University, School of Physics and Astronomy, Tel Aviv 69978, Israel*
[64]*University of Tennessee, Knoxville, Tennessee 37996, USA*
[65]*University of Texas at Austin, Austin, Texas 78712, USA*
[66]*University of Texas at Dallas, Richardson, Texas 75083, USA*
[67a]*INFN Sezione di Torino, I-10125 Torino, Italy*
[67b]*Dipartimento di Fisica, Università di Torino, I-10125 Torino, Italy*
[68a]*INFN Sezione di Trieste, I-34127 Trieste, Italy*
[68b]*Dipartimento di Fisica, Università di Trieste, I-34127 Trieste, Italy*
[69]*IFIC, Universitat de Valencia-CSIC, E-46071 Valencia, Spain*
[70]*University of Victoria, Victoria, British Columbia, Canada V8W 3P6*
[71]*Department of Physics, University of Warwick, Coventry CV4 7AL, United Kingdom*
[72]*University of Wisconsin, Madison, Wisconsin 53706, USA*
(Received 22 June 2015; published 2 October 2017)

We report a Dalitz plot analysis of charmless hadronic decays of charged B mesons to the final state $K^0_S\pi^+\pi^0$ using the full *BABAR* data set of 470.9 ± 2.8 million $B\bar{B}$ events collected at the $\Upsilon(4S)$ resonance. We measure the overall branching fraction and CP asymmetry to be $\mathcal{B}(B^+ \to K^0\pi^+\pi^0) = (31.8 \pm 1.8 \pm 2.1^{+6.0}_{-0.0}) \times 10^{-6}$ and $A_{CP}(B^+ \to K^0\pi^+\pi^0) = 0.07 \pm 0.05 \pm 0.03^{+0.02}_{-0.03}$, where the uncertainties are statistical, systematic, and due to the signal model, respectively. This is the first measurement of the branching fraction for $B^+ \to K^0\pi^+\pi^0$. We find first evidence of a CP asymmetry in $B^+ \to K^*(892)^+\pi^0$ decays: $A_{CP}(B^+ \to K^*(892)^+\pi^0) = -0.52 \pm 0.14 \pm 0.04^{+0.04}_{-0.02}$. The significance of this asymmetry, including systematic and model uncertainties, is 3.4 standard deviations. We also measure the branching fractions and CP asymmetries for three other intermediate decay modes.

DOI: 10.1103/PhysRevD.96.072001

I. INTRODUCTION

The Cabibbo-Kobayashi-Maskawa (CKM) mechanism [1,2] for quark mixing describes all weak charged current transitions between quarks in terms of a unitarity matrix with four parameters: three rotation angles and an irreducible phase. The unitarity of the CKM matrix is usually expressed as triangle relationships among its elements. The interference between tree-level and loop ("penguin") amplitudes can give rise to direct CP violation, which is sensitive to the angles of the Unitarity Triangle, denoted α, β, and γ. Measurements of the parameters of the CKM matrix provide an important test of the Standard Model (SM) since any deviation from unitarity or discrepancies between measurements of the same parameter in different decay processes would imply a possible signature of new physics. Tree amplitudes in $B \to K^*\pi$ decays are sensitive to γ, which can be extracted from interferences between the intermediate states that populate the $K\pi\pi$ Dalitz plane. However, these amplitudes are Cabibbo-suppressed relative to contributions carrying a different phase and involving radiation of either a gluon (QCD penguin) or photon (electroweak penguin or EWP) from a loop.

QCD penguin contributions can be eliminated by constructing a linear combination of the weak decay amplitudes for $B^+ \to K^*\pi$ to form a pure isospin $I = \frac{3}{2}$ state [3]:

$$A_{\frac{3}{2}} = A(K^{*0}\pi^+) + \sqrt{2}A(K^{*+}\pi^0). \quad (1)$$

[*]Deceased.
[†]Now at: University of Tabuk, Tabuk 71491, Saudi Arabia.
[‡]Also at: Università di Perugia, Dipartimento di Fisica, I-06123 Perugia, Italy.
[§]Now at: Laboratoire de Physique Nucléaire et de Hautes Energies, IN2P3/CNRS, F-75252 Paris, France.
[‖]Now at: University of Huddersfield, Huddersfield HD1 3DH, UK.
[¶]Now at: University of South Alabama, Mobile, Alabama 36688, USA.
[**]Also at: Università di Sassari, I-07100 Sassari, Italy.

Since all transitions from $I = \frac{1}{2}$ to $I = \frac{3}{2}$ states occur via only $\Delta I = 1$ operators, $A_{\frac{3}{2}}$ is free from QCD contributions. The weak phase of $A_{\frac{3}{2}}$ is often denoted as

$$\Phi_{\frac{3}{2}} = -\frac{1}{2}\mathrm{Arg}(\bar{A}_{\frac{3}{2}}/A_{\frac{3}{2}}), \tag{2}$$

where $\bar{A}_{\frac{3}{2}}$ is the CP conjugate of the amplitude in Eq. (1). The phase $\Phi_{\frac{3}{2}}$ in Eq. (2) is the CKM angle γ in the absence of EWP contributions [4].

Measurements of the rates and CP asymmetries in $B \to K\pi$ have generated considerable interest because of possible hints of new-physics contributions [5,6]. Of particular interest is the difference, ΔA_{CP}, between the CP asymmetry in $B^+ \to K^+\pi^0$ and the CP asymmetry in $B^0 \to K^+\pi^-$, which in the SM is expected to be consistent with zero within the theoretical uncertainties assuming U-spin symmetry and in the absence of color-suppressed tree and electroweak amplitudes [7,8]. Using the average values of A_{CP} of $K^+\pi^0$ and $K^+\pi^-$ decays [9], $\Delta A_{CP}(K\pi)$ is

$$\begin{aligned}\Delta A_{CP}(K\pi) &= A_{CP}(K^+\pi^0) - A_{CP}(K^+\pi^-) \\ &= 0.122 \pm 0.022,\end{aligned} \tag{3}$$

which differs from zero by 5.5 standard deviations. Unfortunately, hadronic uncertainties prevent a clear interpretation of these results in terms of the new-physics implications [3,10]. Additional information can be obtained through studies of the related vector-pseudoscalar decays $B \to K^*\pi$ and $B \to K\rho$ [11–13], for which the ratios of tree-to-penguin amplitudes are expected to be two to three times larger than for $B \to K\pi$ decays. Hence, $B \to K^*\pi$ and $B \to K\rho$ decays could have considerably larger CP asymmetries.

In this article, we present the results from an amplitude analysis of $B^+ \to K^0_S\pi^+\pi^0$ decays. The inclusion of charge conjugate processes is implied throughout this article, except when referring to CP asymmetries. This is the first Dalitz plot analysis of this decay by *BABAR*; the only previous *BABAR* analysis of this decay was restricted to measuring the branching fraction and CP asymmetry of $B^+ \to K^0\rho^+$ [14]. An upper limit on the branching fraction for $B^+ \to K^0\pi^+\pi^0$ was set by the CLEO Collaboration: $\mathcal{B}(B^+ \to K^0\pi^+\pi^0) < 66 \times 10^{-6}$ [15].

Two contributions to the $K^0_S\pi^+\pi^0$ final state arise from the resonant decays $B^+ \to K^*(892)^0\pi^+$ and $B^+ \to K^*(892)^+\pi^0$. Although both the rate and CP asymmetries for $B^+ \to K^*(892)^0\pi^+$ have been well measured, with $K^{*0} \to K^+\pi^-$, by both the *BABAR* [16] and Belle [17] Collaborations, the measurements of the rate and CP asymmetry for $B^+ \to K^*(892)^+\pi^0$ [18] have significant statistical uncertainties and could benefit from the additional information provided by a full amplitude analysis. In Table I we review the existing measurements of the rates and CP asymmetries in the $B \to K^*(892)\pi$ system.

TABLE I. Average values of the branching fractions $\mathcal{B}$ and CP asymmetries A_{CP} for $B \to K^*(892)\pi$ decays as determined by the Heavy Flavor Averaging Group [9].

Mode	$\mathcal{B}(10^{-6})$	A_{CP}	References
$K^{*+}\pi^-$	8.5 ± 0.7	-0.23 ± 0.06	[19–22]
$K^{*+}\pi^0$	8.2 ± 1.8	-0.06 ± 0.24	[18]
$K^{*0}\pi^+$	$9.9^{+0.8}_{-0.9}$	-0.038 ± 0.042	[16,17]
$K^{*0}\pi^0$	2.5 ± 0.6	-0.15 ± 0.13	[19,23]

This article is organized as follows. The isobar model used to parametrize the complex amplitudes describing the intermediate resonances contributing to the $K^0_S\pi^+\pi^0$ final state is presented in Sec. II. A brief description of the *BABAR* detector and the data set is given in Sec. III. The event reconstruction and selection are discussed in detail in Sec. IV, the background study in Sec. V, and a description of the extended maximum likelihood fit in Sec. VI. The results are given in Sec. VII, and a study of the systematic uncertainties is presented in Sec. VIII. In Sec. IX, we provide a summary and conclusion, discussing the results and combining the branching fractions and CP asymmetries for the decays $B^+ \to K^*(892)^0\pi^+$, $B^+ \to K^*_0(1430)^0\pi^+$, and $B^+ \to K^*(892)^+\pi^0$ with previous *BABAR* results obtained from the final states $B^+ \to K^+\pi^-\pi^+$ and $B^+ \to K^+\pi^0\pi^0$.

II. AMPLITUDE ANALYSIS FORMALISM

A number of intermediate states contribute to the decay $B^+ \to K^0_S\pi^+\pi^0$. Their individual contributions are measured by performing a maximum likelihood fit to the distribution of events in the Dalitz plot formed from the two variables, $m^2_{K^0_S\pi^+}$ and $m^2_{\pi^+\pi^0}$. We use the `Laura++` [24] software to perform this fit.

The total signal amplitudes for the B^+ and the B^- decays are given in the isobar formalism by [25,26]

$$A(m^2_{K^0_S\pi^+}, m^2_{\pi^+\pi^0}) = \sum_j c_j F_j(m^2_{K^0_S\pi^+}, m^2_{\pi^+\pi^0}), \tag{4}$$

$$\bar{A}(m^2_{K^0_S\pi^-}, m^2_{\pi^-\pi^0}) = \sum_j \bar{c}_j \bar{F}_j(m^2_{K^0_S\pi^-}, m^2_{\pi^-\pi^0}), \tag{5}$$

where c_j is the complex coefficient for a given resonant decay mode j contributing to the Dalitz plot. This complex coefficient contains the weak-interaction phase dependence that is measured relative to one of the contributing resonant channels. In this article we report results for the relative phases between each pair of amplitudes.

The function F_j describes the dynamics of the decay amplitudes and is the product of a resonant line shape (R_j),

two Blatt-Weisskopf barrier factors [27] (X_L), and an angular-dependent term ($T_{j,L}$) [28]:

$$F_j = R_j \times X_L(|\vec{p}|,|\vec{p}_0|) \times X_L(|\vec{q}|,|\vec{q}_0|) \times T_{j,L}(\vec{p},\vec{q}), \quad (6)$$

where L is the orbital angular momentum between the intermediate resonance and the bachelor particle (the bachelor particle is the daughter of the B decay that does not arise from the resonance), $\vec{q}$ is the momentum of one of the daughters of the resonance in the rest frame of the resonance, $\vec{p}$ is the momentum of the bachelor particle in the rest frame of the resonance, and $\vec{p}_0$ and $\vec{q}_0$ are the values of $\vec{p}$ and $\vec{q}$, respectively, at the nominal mass of the resonance. The Blatt-Weisskopf barrier factors are given by

$$X_{L=0}(|\vec{u}|,|\vec{u}_0|) = 1, \quad (7)$$

$$X_{L=1}(|\vec{u}|,|\vec{u}_0|) = \sqrt{\frac{1+z_0}{1+z}}, \quad (8)$$

$$X_{L=2}(|\vec{u}|,|\vec{u}_0|) = \sqrt{\frac{(z_0-3)^2+9z_0}{(z-3)^2+9z}}, \quad (9)$$

where $z = (|\vec{u}|r_{\rm BW})^2$, $z_0 = (|\vec{u}_0|r_{\rm BW})^2$, $\vec{u}$ is either $\vec{q}$ or $\vec{p}$, and $r_{\rm BW} = 4.0\ (\mathrm{GeV}/c)^{-1}$ is the meson radius parameter. The uncertainty in $r_{\rm BW}$, used for systematic variations, is $\pm 2\ (\mathrm{GeV}/c)^{-1}$ for the K^* resonances, and ranges from -1.0 to $+2.0\ (\mathrm{GeV}/c)^{-1}$ for the $\rho(770)^+$ [28]. The angular term depends on the spin of the resonance and is given by [29,30]

$$T_{j,L=0} = 1, \quad (10)$$

$$T_{j,L=1} = -2\vec{p}.\vec{q}, \quad (11)$$

$$T_{j,L=2} = \frac{4}{3}[3(\vec{p}.\vec{q})^2 - (|\vec{p}||\vec{q}|)^2]. \quad (12)$$

The choice of which resonance daughter is defined to carry the momentum $\vec{q}$ is a matter of convention. However, its definition is important when comparing measurements from different experiments. In Fig. 1, we illustrate the momentum definitions used for the $K^0_S\pi^+$, $K^0_S\pi^0$, and $\pi^+\pi^0$ resonance combinations.

Table II lists the resonances used to model the signal. We determine a nominal model from data by studying changes in the log likelihood values for the best fit when omitting or adding a resonance to the fit model, as described in Sec. VI.

For the $K^*(892)^0$ and $K^*(892)^+$ resonances, we use a relativistic Breit-Wigner (RBW) line shape [28]:

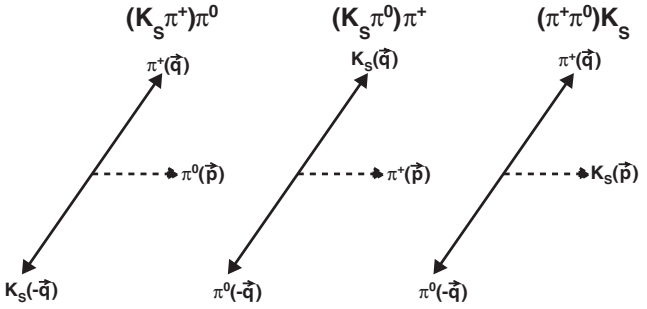

FIG. 1. Schematic representation of the definitions of $\vec{q}$ and $\vec{p}$ used in this analysis for the (left) $K^0_S\pi^+$, (center) $K^0_S\pi^0$, and (right) $\pi^+\pi^0$ resonances.

$$R_j^{\rm RBW}(m) = \frac{1}{m_0^2 - m^2 - im_0\Gamma(m)}, \quad (13)$$

where m is the two-body invariant mass and $\Gamma(m)$ is the mass-dependent width. In general, for a resonance decaying to spin-0 particles, $\Gamma(m)$ can be expressed as

$$\Gamma(m) = \Gamma_0\left(\frac{|\vec{q}|}{|\vec{q}_0|}\right)^{2L+1}\left(\frac{m_0}{m}\right)X_L(|\vec{q}|,|\vec{q}_0|)^2, \quad (14)$$

where m_0 and Γ_0 are the nominal mass and width of the resonance.

The Gounaris-Sakurai (GS) parametrization [34] is used to describe the line shape of the ρ resonance decaying into two pions. The parametrization takes the form

$$R_j^{\rm GS} = \frac{1+\Gamma_0\cdot d/m_0}{m_0^2 - m^2 + f(m) - im_0\Gamma(m)}, \quad (15)$$

TABLE II. Parameters of the Dalitz plot model for $B^+ \to K^0_S\pi^+\pi^0$ used in the nominal fit. The mass and width of the $\rho(770)^+$ and their uncertainties are taken from the analyses by the ALEPH [31] and CMD2 [32] Collaborations. All other parameters are taken from Ref. [28]. The resonance shapes are a Gounaris-Sakurai (GS) function, a relativistic Breit-Wigner (RBW) function, or based on measurements by the LASS Collaboration [33], with a the scattering length and r the effective range of the LASS parametrization.

		Parameters	
		Resonance mass	Width
Resonance	Line shape	(MeV/c^2)	(MeV)
$\rho(770)^+$	GS	775.5 ± 0.6	148.2 ± 0.8
$K^*(892)^+$	RBW	891.7 ± 0.3	50.8 ± 0.9
$K^*(892)^0$	RBW	896.1 ± 0.2	50.7 ± 0.6
$(K\pi)_0^{*0/+}$	LASS	1412 ± 50	294 ± 80
		$m_{\rm cutoff} = 1800\ \mathrm{MeV}/c^2$ [16]	
		$a = 2.1 \pm 0.1\ (\mathrm{GeV}/c)^{-1}$ [16]	
		$r = 3.3 \pm 0.3\ (\mathrm{GeV}/c)^{-1}$ [16]	

where $\Gamma(m)$ is given by Eq. (14). Expressions for $f(m)$, in terms of Γ_0 and m, and the constant d can be found in Ref. [34]. The parameters specifying the ρ line shape are taken from Refs. [31,32], which provides line shape information derived from fits to e^+e^- annihilation and τ lepton decay data.

For the $J^P = 0^+$ component of the $K\pi$ spectrum, denoted $(K\pi)_0^{*0/+}$, we make use of the LASS parametrization [33], which consists of a K_0^* resonant term together with an effective-range, nonresonant component to describe the slowly increasing phase as a function of the $K\pi$ mass:

$$R_j^{\rm LASS} = e^{2i\delta_B}\frac{m_0\Gamma_0\frac{m_0}{|\vec{q}_0|}}{(m_0^2-m^2)-im_0\Gamma_0\frac{|\vec{q}|m_0}{m|\vec{q}_0|}}+\frac{m}{|\vec{q}|\cot\delta_B - i|\vec{q}|}, \tag{16}$$

where $\cot\delta_B = \frac{1}{a|\vec{q}|}+\frac{1}{2}r|\vec{q}|$. The values used for the scattering length a and the effective range r are given in Table II. The effective-range component has a cutoff imposed at 1800 MeV/c^2 [16]. Integrating separately the resonant term, the effective-range term, and the coherent sum, we find that the resonant terms (hereafter referred to as the $K^*{}_0(1430)^0$ and the $K^*{}_0(1430)^+$) account for 88% of the sum, and the effective range component 49%; the 37% excess is due to destructive interference between the two terms. The LASS parametrization is the least well-determined component of the signal model; we discuss the impact of these uncertainties in Sec. VIII.

The complex coefficients c_j and $\bar{c}_j$ in Eqs. (4), (5) can be parametrized in different ways; we follow the parametrization used in Ref. [16] as it avoids a bias in the measurement of amplitudes and phases when the resonant components have small magnitudes:

$$\begin{aligned} c_j &= (x_j+\Delta x_j)+i(y_j+\Delta y_j),\\ \bar{c}_j &= (x_j-\Delta x_j)+i(y_j-\Delta y_j), \end{aligned} \tag{17}$$

where $x_j \pm \Delta x_j$ and $y_j \pm \Delta y_j$ are the real and imaginary parts of the amplitudes. The quantities Δx_j and Δy_j parametrize the CP violation in the decay. The CP asymmetry for a given intermediate state is given by

$$A_{CP,j} = \frac{|\bar{c}_j|^2-|c_j|^2}{|\bar{c}_j|^2+|c_j|^2} \tag{18}$$

$$= -\frac{2(x_j\Delta x_j + y_j\Delta y_j)}{x_j^2+\Delta x_j^2+y_j^2+\Delta y_j^2}. \tag{19}$$

The results quoted for the resonances in the following analysis use fit fractions (FF_j) as phase-convention-independent quantities representing the fractional rate of each contribution in the Dalitz plot. The FF for mode j is defined as

$$\mathrm{FF}_j = \frac{\iint(|c_jF_j|^2+|\bar{c}_j\bar{F}_j|^2)dm_{K\pi}^2dm_{\pi\pi}^2}{\iint(|A|^2+|\bar{A}|^2)dm_{K\pi}^2dm_{\pi\pi}^2}. \tag{20}$$

The sum of all the fit fractions does not necessarily yield unity due to constructive and destructive interference, as quantified by the interference fit fractions given by [30]

$$\mathrm{FF}_{ij} = \frac{\iint 2\mathrm{Re}[c_ic_j^*F_iF_j^*]dm_{K\pi}^2dm_{\pi\pi}^2}{\iint|\sum_k c_kF_k|^2dm_{K\pi}^2dm_{\pi\pi}^2}. \tag{21}$$

The parameters x_j, Δx_j, y_j, and Δy_j are determined in the fit, except for the reference amplitude. Fit fractions, relative phases, and asymmetries are derived from the fit parameters and their statistical uncertainties determined from pseudo experiments generated from the fit results.

III. THE *BABAR* DETECTOR AND MC SIMULATION

The data used in the analysis were collected with the *BABAR* detector at the PEP-II asymmetric-energy e^+e^- collider at SLAC National Accelerator Laboratory. The sample consists of 429 fb^{-1} of integrated luminosity recorded at the $\Upsilon(4S)$ resonance mass ("on-peak") and 45 fb^{-1} collected 40 MeV below the resonance mass ("off-peak") [35]. The on-peak sample corresponds to the full *BABAR* $\Upsilon(4S)$ data set and contains 470.9 ± 2.8 million $B\bar{B}$ events [30]. A detailed description of the *BABAR* detector is given in Refs. [36,37]. Charged-particle tracks are measured by means of a five-layer double-sided silicon vertex tracker (SVT) and a 40-layer drift chamber (DCH), both positioned within a solenoid that provides a 1.5 T magnetic field. Charged-particle identification is achieved by combining the information from a ring-imaging Cherenkov detector (DIRC) and specific ionization energy loss ($\mathrm{d}E/\mathrm{d}x$) measurements from the DCH and SVT. Photons are detected and their energies measured in a CsI(Tl) electromagnetic calorimeter (EMC). Muon candidates are identified in the instrumented flux return of the solenoid.

We use GEANT4-based software to simulate the detector response and account for the varying beam and experimental conditions [38,39]. The `EvtGen` [40] and `Jetset 7.4` [41] software packages are used to generate signal and background Monte-Carlo (MC) event samples in order to determine efficiencies and evaluate background contributions for different selection criteria.

IV. EVENT SELECTION

We reconstruct $B^+ \to K_S^0\pi^+\pi^0$ candidates from one π^0 candidate, one K_S^0 candidate reconstructed from a pair of oppositely charged pions, and a charged pion candidate.

The π^0 candidate is formed from a pair of neutral energy clusters in the EMC with laboratory energies above 0.05 GeV and lateral moments [42] between 0.01 and 0.6. We require the invariant mass of the reconstructed π^0 to lie in the range $0.11 < m_{\gamma\gamma} < 0.16$ GeV/c^2. The K^0_S candidate is required to have a $\pi^+\pi^-$ invariant mass within 15 MeV/c^2 of the K^0_S mass [28], and a proper decay time greater than 0.5×10^{-11} s. To reduce combinatorial background, we also require that the K^0_S candidates have a vertex probability greater than 10^{-6} and that the cosine of the angle between the K^0_S momentum direction and the K^0_S flight direction (as determined by the interaction point and the K^0_S vertex) be greater than 0.995. For the π^+ candidate, we use information from the tracking systems, the EMC, and the DIRC to select a charged track consistent with the pion hypothesis. We constrain the π^+ track and K^0_S candidate to originate from a common vertex.

Signal events that are misreconstructed with the decay products of one or more daughters completely or partially exchanged with other particles in the rest of the event have degraded kinematic resolution. We refer to these as "self-cross-feed" (SCF) events. This misreconstruction has a strong dependence on the energy of the particles concerned and is more frequent for low-energy particles, *i.e.*, for decays in the corners of the Dalitz plot. Because of the presence of a π^0 in the final state, there is a significant probability for signal events to be misreconstructed due to low-energy photons from the π^0 decay. Using a classification based on MC information, we find that in simulated events the SCF fraction depends strongly on the resonant substructure of the signal and ranges from 34% for $B^+ \to K^*(892)^+\pi^0$ to 50% for $B^+ \to \rho(770)^+K^0_S$. In events simulated uniformly in phase space, hereafter referred to as nonresonant MC, the SCF fraction varies from less than 10% in the center of the Dalitz plot to almost 70% in the two corners of the Dalitz plot, where either the π^0 or the π^+ has low energy. We describe how the SCF events are handled in Sec. VI.

In order to suppress the dominant background, due to continuum $e^+e^- \to q\bar{q}(q = u, d, s, c)$ events, we employ a boosted decision tree (BDT) algorithm that combines four variables commonly used to discriminate jetlike $q\bar{q}$ events from the more spherical $B\bar{B}$ events in the e^+e^- center-of-mass (CM) frame. The first of these is the ratio of the second-to-zeroth order momentum-weighted Legendre polynomial moments,

$$\frac{L_2}{L_0} = \frac{\sum_{i\in\mathrm{ROE}} \frac{1}{2}(3\cos^2\theta_i - 1)p_i}{\sum_{i\in\mathrm{ROE}} p_i}, \tag{22}$$

where the summations are over all tracks and neutral clusters in the event, excluding those that form the B candidate (the "rest of the event" or ROE); p_i is the particle momentum, and θ_i is the angle between the particle and the thrust axis of the B candidate, hereafter also referred to as the B. The three other variables entering the BDT are the absolute value of the cosine of the angle between the B direction and the collision axis, the zeroth-order momentum-weighted Legendre polynomial moment, and the absolute value of the output of another BDT used for "flavor tagging," *i.e.*, for distinguishing B from $\bar{B}$ decays using inclusive properties of the decay of the other B meson in the $\Upsilon(4S) \to B\bar{B}$ event [43]. Although flavor tagging is not needed for charged B decays, the degree of tagging certainty provides some discrimination between $B\bar{B}$ pairs and continuum background. The momentum-weighted Legendre polynomial moments and the cosine of the angle between the B direction and the beam axis are calculated in the e^+e^- CM frame. The BDT is trained on a sample of signal MC events and off-peak data. We apply a loose criterion on the BDT output of $\mathrm{BDT_{out}} > 0.06$, which retains approximately 70% of the signal while rejecting 92% of the $q\bar{q}$ background.

In addition to $\mathrm{BDT_{out}}$, we use two kinematic variables to distinguish the signal from the background:

$$m_{\mathrm{ES}} = \sqrt{E^2_{\mathrm{X}} - \mathbf{p}^2_B}, \tag{23}$$

$$\Delta E = E^\star_B - \sqrt{s}/2, \tag{24}$$

where

$$E_{\mathrm{X}} = (s/2 + \mathbf{p}_{e^+e^-} \cdot \mathbf{p}_B)/E_{e^+e^-}, \tag{25}$$

and where $\sqrt{s}$ is the total e^+e^- CM energy, with $(E_{e^+e^-}, \mathbf{p}_{e^+e^-})$ and $(E_B, \mathbf{p}_B)$ the four-momenta of the initial e^+e^- system and the B candidate, respectively, both measured in the lab frame. The quantity $E^\star_B$ is the energy of the B candidate measured in the e^+e^- CM frame. The signal m_{ES} distribution for correctly reconstructed events is approximately independent of their position in the $K^0_S\pi^+\pi^0$ Dalitz plot and peaks near the B mass with a resolution of about 3.4 MeV/c^2.

We retain all candidates satisfying the following selection criteria: $5.23 < m_{\mathrm{ES}} < 5.29$ GeV/c^2 and $-0.3 < \Delta E < 0.3$ GeV. The signal region, where the final fit to data is performed, is defined by the tighter criteria $5.260 < m_{\mathrm{ES}} < 5.287$ GeV/c^2 and $-0.20 < \Delta E < 0.15$ GeV. We also use candidates in the sideband region of m_{ES} defined by $5.23 < m_{\mathrm{ES}} < 5.26$ GeV/c^2 and $-0.20 < \Delta E < 0.15$ GeV and subtract the $B\bar{B}$ background contributions, predicted by MC simulations, from the distribution for these sideband events. We then add these distributions to the off-peak data distributions to increase the statistical precision of our model of the Dalitz plot distribution for continuum background.

Each of the B candidates is refit to determine the Dalitz plot variables. In these fits the $K^0_S\pi^+\pi^0$ invariant mass is constrained to the world average value of the B mass [28] to improve position resolution within the Dalitz plot.

We find that 20% of the remaining events in nonresonant MC have two or more candidates. We choose the best candidate in multiple-candidate events based on the highest B-vertex probability. This procedure is found to select a correctly reconstructed candidate more than 60% of the time and does not bias the fit variables.

The reconstruction efficiency over the Dalitz plot is modeled using a two-dimensional (2D) binned distribution based on a generated sample of approximately 2×10^6 simulated $B^+\to K^0_S\pi^+\pi^0$ MC events, where the events uniformly populate phase space. All selection criteria are applied except for those corresponding to a $K\pi$ invariant-mass veto described below, which is taken into account separately. The 2D histogram of reconstructed MC events is then divided by the 2D histogram of the generated MC events. In order to expand regions of phase space with large efficiency variations, the Dalitz plot variables are transformed into "square Dalitz plot" [44] coordinates. We obtain an average efficiency, for nonresonant MC events, of approximately 15%. In the likelihood fit we use an event-by-event efficiency that depends on the Dalitz plot position.

V. $B\bar{B}$ BACKGROUNDS

In addition to continuum events, background arises from nonsignal $B\bar{B}$ events. A major source of $B\bar{B}$ background arises from $B^+\to\bar{D}^0(\to K^0_S\pi^0)\pi^+$ decays. To suppress this background, we veto events with $1.804<m_{K^0_S\pi^0}<1.924\,\mathrm{GeV}/c^2$.

The remaining $B\bar{B}$ backgrounds are studied using MC simulations and classified based on the shape of the $m_{\rm ES}$, ΔE, and Dalitz plot distributions. We identify nine categories of $B\bar{B}$ backgrounds: categories 1, 2 and 3 include different types of three- and four-body B decays involving an intermediate D meson; categories 4 and 5 include charmless four-body B decays to intermediate resonances where a π^0 in the final state is not reconstructed; categories 6 and 7 include two-body B decays with a radiated photon misreconstructed as a π^0 decay product or where the π^0 arises from the other B decay; category 8 includes charmless three-body B decays where a charged pion is interchanged with a π^0 meson from the other B; and finally category 9 includes all other simulated $B\bar{B}$ background contributions. Within each category, each of the $m_{\rm ES}$, ΔE, $\mathrm{BDT_{out}}$, and Dalitz plot distributions are formed by combining the contributions of all decay modes in the category. The combinations are done by normalizing the distributions for each decay mode to the expected number of events in the recorded data sample, which is estimated using reconstruction efficiencies determined from MC, the number of $B\bar{B}$ pairs in the recorded data sample, and the branching fractions listed in Refs. [9,28]. For each category, the histograms of $m_{\rm ES}$, ΔE, $\mathrm{BDT_{out}}$, and the Dalitz plot variables are used as the probability density functions (PDF) in the likelihood fit to data to model the $B\bar{B}$ background.

VI. THE MAXIMUM LIKELIHOOD FIT

The extended likelihood function is given by

$$\mathcal{L}=\exp\left(-\sum_k N_k\right)\times\prod_{i=1}^{N_e}\left[\sum_k N_k\mathcal{P}_k^i(m^2_{K^0_S\pi^+},m^2_{\pi^+\pi^0},m_{\rm ES},\Delta E,\mathrm{BDT_{out}},q_B)\right],\tag{26}$$

where N_k is the number of candidates in each signal or background category k, N_e is the total number of events in the data sample, and $\mathcal{P}_k^i$ (the PDF for category k and event i) is the product of the PDFs describing the Dalitz plot, $m_{\rm ES}$, ΔE, and $\mathrm{BDT_{out}}$ distributions, with q_B the charge of the B candidate.

To avoid possible biases in the determination of the fit parameters [45], we use MC samples to study correlations between the fit variables and the Dalitz plot parameters, $m^2_{K^0_S\pi^+}$ and $m^2_{\pi^+\pi^0}$. We find that for correctly reconstructed signal candidates, the ΔE distribution is strongly dependent on $m_{K^0_S\pi^+}$. This is mostly due to a dependence of the energy resolution of the B candidate on the π^0 momentum. For SCF signal candidates, both the $m_{\rm ES}$ and ΔE distributions depend on all three two-body invariant masses: $m_{K^0_S\pi^+}$, $m_{K^0_S\pi^0}$, and $m_{\pi^+\pi^0}$. The $m_{\rm ES}$, ΔE, and $\mathrm{BDT_{out}}$ distributions for continuum and $B\bar{B}$ backgrounds have negligible correlations with the Dalitz plot parameters.

For correctly reconstructed signal candidates, the $m_{\rm ES}$ and ΔE PDFs are parameterized by a Cruijff function, which is given by (omitting normalization factor)

$$f_{\rm Cruijff}(x)=\exp\left[\frac{-(x-m)^2}{2\sigma^2_{L,R}+\alpha_{L,R}(x-m)^2}\right],\tag{27}$$

where m gives the peak of the distribution and the asymmetric width of the distribution is given by σ_L for $x<m$ and σ_R for $x>m$. The asymmetric modulation is similarly given by α_L for $x<m$ and α_R for $x>m$. The ΔE PDF parameters are calculated on an event-by-event basis in terms of the $K^0_S\pi^+$ invariant mass, as a linear function for $m^2_{K^0_S\pi^+}<20\ \mathrm{GeV}^2/c^4$ and as a quadratic function for $m^2_{K^0_S\pi^+}>20\ \mathrm{GeV}^2/c^4$. These functions are determined by fitting the ΔE distribution in large nonresonant MC

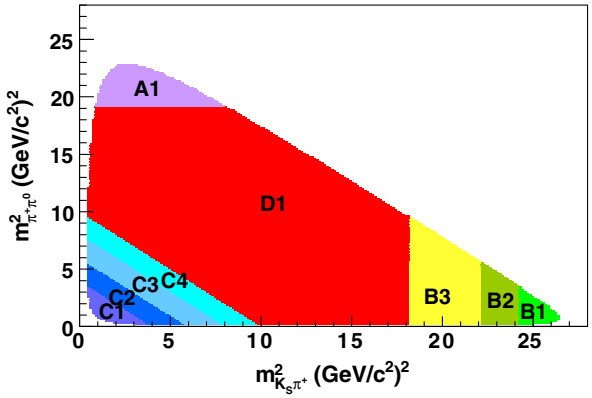

FIG. 2. Diagram illustrating the division of the Dalitz plot into different regions for the definition of the PDFs for self cross feed signal events. Each letter indicates whether the dependence is on $m^2_{\pi^+\pi^0}$ (A), $m^2_{K^0_S\pi^+}$ (B), or $m^2_{K^0_S\pi^0}$ (C). The remaining region of the Dalitz plot (D1) is where we expect to find fewer SCF events, and where the shapes for $m_{\rm ES}$ and ΔE are less dependent on their position in the Dalitz plot, further described in Table III.

samples. For the SCF signal, in order to follow the rapid shape variations across the Dalitz plot of the $m_{\rm ES}$ and ΔE distributions, we divide the Dalitz plot into several regions as illustrated in Fig. 2. Each letter indicates whether the dependence is on $m^2_{\pi^+\pi^0}$, $m^2_{K^0_S\pi^+}$, or $m^2_{K^0_S\pi^0}$. The regions are chosen based on the distribution in the Dalitz plot of the SCF fraction and the mean difference between the true and reconstructed position in the Dalitz plot; we include more regions in areas of the Dalitz plot where these quantities are largest. As a representative example of the variation in ΔE distribution in nonresonant signal MC simulation, we show in Fig. 3 the ΔE distributions for regions C1, C2, C3, and

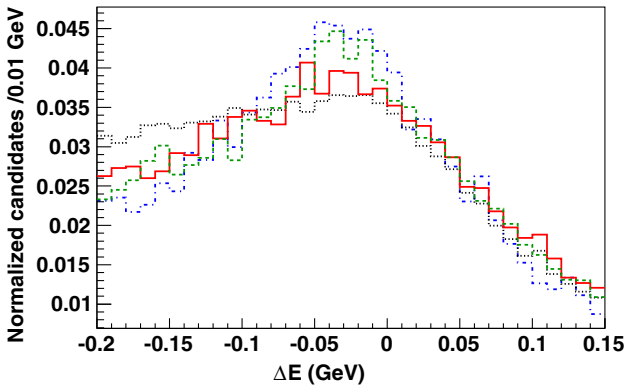

FIG. 3. Variations of the ΔE distribution as seen in nonresonant signal MC simulation across the $m^2_{K^0_S\pi^0}$ regions (bands starting with label C in Fig. 2). The dotted (black) histogram shows the distribution in region C1, the solid (red) histogram the distribution in region C2, the dashed (green) histogram the distribution in region C3, and the dash-dotted (blue) histogram the distribution in region C4.

TABLE III. List of PDFs used to describe the $m_{\rm ES}$ and ΔE self cross feed signal distributions in each of the regions of the $B^+ \to K^0_S\pi^+\pi^0$ Dalitz plot shown in Fig. 2. The abbreviations correspond to the following functional forms: Cruijff function described in Eq. (27) (Cruijff), Chebychev polynomial (Cheb), Gaussian (Gauss), two-piece Gaussian described in Eq. (28) (BGauss), and exponential (Exp).

Dalitz plot region	$m_{\rm ES}$ PDF	ΔE PDF
$m^2_{\pi^+\pi^0}$ (A1)	Cruijff	Cruijff
$m^2_{K^0_S\pi^+}$ (B1)	Cheb + Gauss	Exp + Sigmoid
(B2)	Cheb + Gauss	linear + BGauss
(B3)	Cruijff	Exp + Sigmoid
$m^2_{K^0_S\pi^0}$ (C1)	Cheb + Gauss	Cheb
(C2)	Cheb + Gauss	Cheb
(C3)	Cruijff	Cheb
(C4)	Cruijff	Cruijff
Central region (D1)	Cruijff	Cruijff

C4. We use $m_{\rm ES}$ and ΔE PDFs specific to each region, as listed in Table III. Some of the PDFs used in the parametrization of the SCF include Cruijff functions, Chebychev polynomials, Gaussian functions, and two-piece Gaussian (BGauss) functions. A two-piece Gaussian function is an asymmetric Gaussian described by the following functional form (omitting normalization factor)

$$f_{\rm BGauss}(x) = \exp\left[\frac{-(x-m)^2}{2\sigma^2_{L,R}}\right]. \quad (28)$$

For the continuum background, we use an ARGUS function [46] to parameterize the $m_{\rm ES}$ shape. The ΔE distribution is described by a linear function, and the $\mathrm{BDT_{out}}$ distribution by an exponential function. The $m_{\rm ES}$, ΔE, and $\mathrm{BDT_{out}}$ PDFs for $B\bar{B}$ backgrounds are defined by the sum of the histograms from the MC simulations for decay modes in each background category, as described in Sec. V.

The continuum and $B\bar{B}$ background Dalitz plot distributions are included in the likelihood as two-dimensional histograms. For $B\bar{B}$ backgrounds, we use MC samples. For continuum background, we combine events from the off-peak data and the $m_{\rm ES}$ sideband in on-peak data, after subtracting contributions from B decays, as described in Sec. IV. For the 2D histograms, we use the square Dalitz plot coordinates. A linear interpolation between bin centers is applied.

The free parameters in the fit are the yields for signal, continuum background, and $B\bar{B}$ background categories 1 and 9. The yields for the remaining $B\bar{B}$ background categories are fixed to the estimated values. All the PDF parameters for the correctly reconstructed $m_{\rm ES}$ and ΔE

PDFs, except for the tail parameters, are determined in the fit. For each region of the Dalitz plot, the SCF fraction is fixed to the value predicted by the nonresonant MC simulation. All SCF signal PDF parameters are fixed to values obtained from fits to nonresonant MC events. The endpoint of the ARGUS function is fixed to 5.289 GeV/c^2 while the shape parameter is determined in the fit. The slope for the linear function of the ΔE PDF and the exponent for the exponential function of the $\mathrm{BDT_{out}}$ PDF for continuum background are similarly determined in the fit. The isobar coefficients, x and y in Eq. (18), for all but one of the isobar components are fitted parameters in the fit and are measured relative to the fixed isobar component. The coefficients for the reference isobar are fixed to $x = 1$ and $y = 0$. In total, the fit is performed with 21 free parameters.

We determine a nominal signal Dalitz plot model based on information from previous studies [16,18–20], and on the changes in the log likelihood in the fit to data when resonances are added to, or removed from, the list shown in Table II. In these fits to the combined B^+ and B^- data samples, the CP coefficients Δx and Δy are fixed to zero. Based on the change in log likelihood and accounting for the change in the number of degrees of freedom when the resonances $\rho(1450)^+$, $K^*{}_2(1430)^0$, $K^*{}_2(1430)^+$, $K^*(1680)^0$, or $K^*(1680)^+$, are added to the default model one at a time, we find that the significance of each resonance is well below 3 sigma. Therefore we do not include any of these additional resonances in the nominal fit. We also note that the fit fractions for these additional resonances, reported in Table IV, are consistent with zero.

We do not observe an excess of events for invariant masses greater than 2 GeV/c^2, suggesting that a nonresonant component, in addition to that included in the LASS parametrization, is not necessary. We observe that if we add a nonresonant component to the fit, the change in log likelihood for the binned data and the fit projections for the $K^0_S\pi^+$, $K^0_S\pi^0$, and $\pi^+\pi^0$ invariant masses are consistent with the expected change due to the additional free parameters in the fit, and do not indicate any statistically significant nonresonant component. We therefore conclude that, with the current level of statistical sensitivity, the base model, which includes the $\rho(770)^+$, $K^*(892)^+$, $K^*(892)^0$, $(K\pi)^{*0}_0$, and $(K\pi)^{*+}_0$ resonances, provides an adequate description of the data.

TABLE IV. Fit fractions obtained from the fit to data when each additional isobar is added to the fit model one at a time.

Additional isobar	Fit fraction
$\rho(1450)^+$	0.042 ± 0.044
$K^*{}_2(1430)^0$	0.038 ± 0.017
$K^*{}_2(1430)^+$	0.012 ± 0.020
$K^*(1680)^0$	0.032 ± 0.034
$K^*(1680)^+$	0.005 ± 0.030

VII. RESULTS

We apply the fit described in Sec. VI to the 31876 selected $B^+ \to K^0_S\pi^+\pi^0$ candidates. A first fit is performed on the combined $B^\pm$ sample. We obtain yields of 1014 ± 60 signal events, 24381 ± 200 continuum events, 2745 ± 70 $B\bar{B}$ events in category 1, and 1768 ± 140 $B\bar{B}$ events in category 9. The results of the fit are shown in Fig. 4. For the purpose of this figure, the contributions of signal events are enhanced by applying the more restrictive selection criteria listed in Table V.

The branching fraction for $B^+ \to K^0\pi^+\pi^0$ is determined from the number of signal events, the efficiency estimated from MC events, and the total number of $B\bar{B}$ events in data. We take into account differences between the π^0 reconstruction efficiency in data and MC events, determined from control samples with either τ leptons or initial-state radiation, as a function of π^0 momentum ($\frac{\epsilon_{\mathrm{data}}}{\epsilon_{\mathrm{MC}}} = 97.2\%$, averaged over π^0 momentum). We correct for small biases in the branching fraction, as determined from MC pseudo experiments generated with the same number of signal events and resonance composition as found in the fit to data. We divide the partial branching fraction of $B^+ \to K^0_S(\to\pi^+\pi^-)\pi^+\pi^0$ by the branching fraction for $K^0_S \to \pi^+\pi^-$, and multiply the result by a factor of 2 to account for K^0_S decay, to obtain the branching fraction result $\mathcal{B}(B^+ \to K^0\pi^+\pi^0) = (31.8 \pm 1.8 \pm 2.1^{+6.0}_{-0.0}) \times 10^{-6}$, where the first uncertainty is statistical, the second is systematic, and the third is due to assumptions made concerning the signal model. The latter two uncertainties are described in Sec. VIII and the breakdown of the systematic uncertainties is detailed in Table XI.

We measure amplitudes and phases relative to each of the five two-body decays in the signal model to take advantage of the smaller uncertainty observed when measuring the relative phases of the two pairs of decays with same-charge K^* resonances. Table VI lists the relative phase, ϕ, between each pair of two-body decays in the signal model and its uncertainty. The statistical uncertainty in the relative phase is smallest ($\approx 10°$) for the resonances that decay to the same-charge $K\pi$ state. This is due to a larger overlap in the Dalitz plot between the same-charge K^* resonances than occurs for other pairs of resonances that only overlap in the corners of the Dalitz plot.

Since the statistical uncertainties of the fit fractions do not depend on the reference mode, we quote in Table VII only the fit fractions from the fit where the $K^*(892)^0\pi^+$ amplitude is the reference. The fit fractions for the $K^*{}_0(1430)^0\pi^+$ and $K^*{}_0(1430)^+\pi^0$ modes are the product of the $(K\pi)^*_0$ S-wave fit fraction, shown in Table VII, and the fraction due to the resonant contribution in the LASS parametrization (88%). The off-diagonal fit

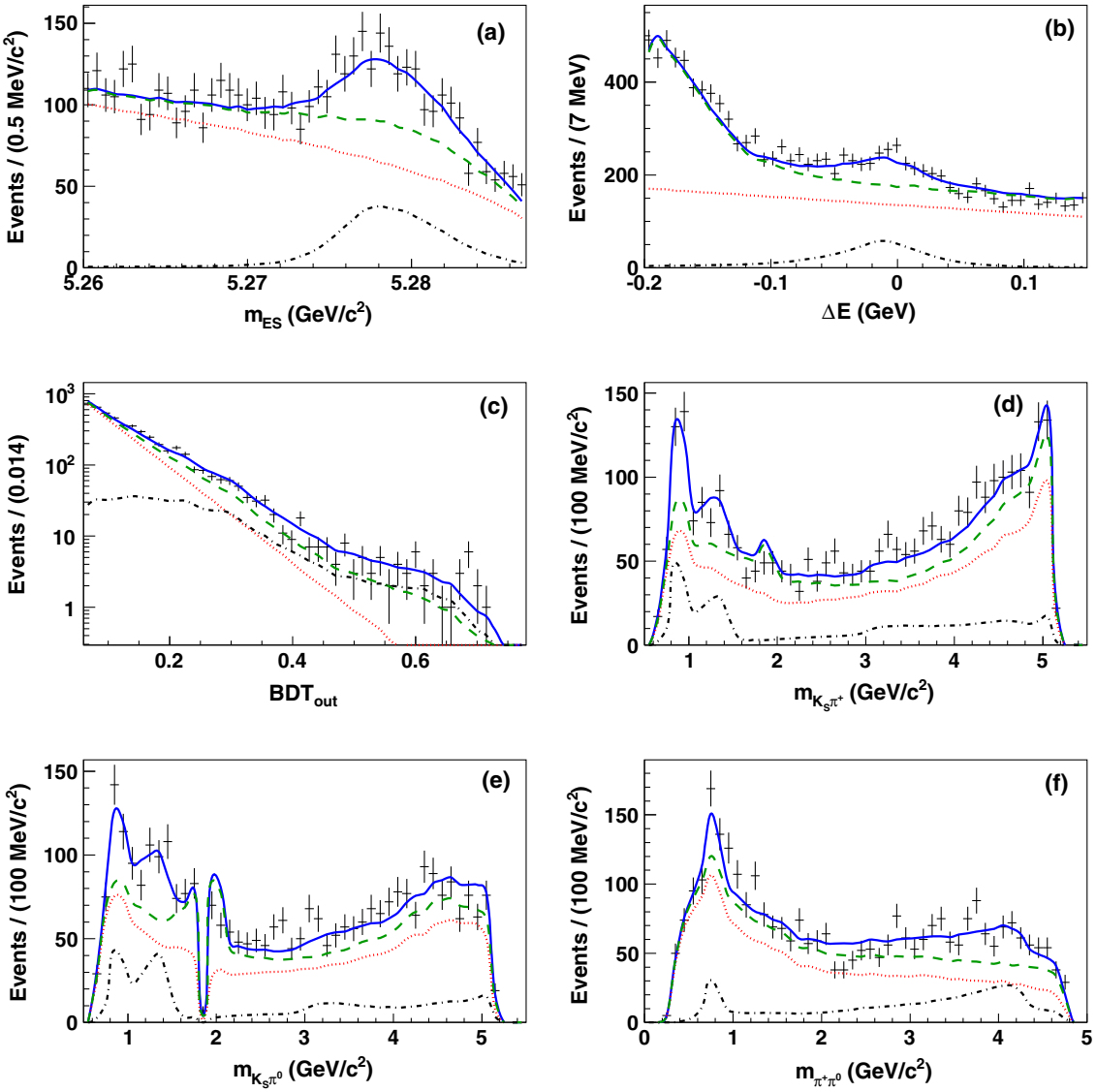

FIG. 4. Combined $B^{\pm}$ fit: Measured distributions and fit projections for $B^{\pm} \to K^0_S\pi^{\pm}\pi^0$ candidates; (a) $m_{\rm ES}$, (b) ΔE, (c) $\mathrm{BDT_{out}}$, (d) $m_{K^0_S\pi^+}$, (e) $m_{K^0_S\pi^0}$, and (f) $m_{\pi^+\pi^0}$. The points with error bars correspond to data, the solid (blue) curves to the total fit result, the dashed (green) curves to the total background contribution, and the dotted (red) curves to the continuum background component. The dash-dotted curves represent the signal contribution. The projected distributions are obtained from statistically precise pseudo experiments generated using the fit results. For all distributions in each panel, the signal-to-background ratio is increased by applying tighter selection requirement on $m_{\rm ES}$, ΔE, and/or $\mathrm{BDT_{out}}$, listed Table V.

fractions are small compared to the diagonal elements. We calculate the branching fractions for the resonant contributions shown in Table VIII as the product of the total branching fraction and the fit fractions returned by the fit to data, including appropriate Clebsch-Gordan coefficients.

To determine the overall *CP* asymmetry as well as the *CP* asymmetries for the contributing isobar components, we simultaneously fit the separate B^+ and B^- data samples. The overall A_{CP} value is calculated from the integrals of the positive and negative signal Dalitz plot distributions. The Δx and Δy parameters from Eq. (18) are allowed to vary in the fit for all components except the reference isobar, for which the Δy parameter is fixed to zero (the relative phase of the B^+ and B^- Dalitz plots cannot be determined since they do not interfere). To account for possible differences in the reconstruction and particle identification efficiencies for B^+ and B^-, the efficiency map as a function of the Dalitz plot position is determined separately for B^+ and B^-. The asymmetry for the continuum background is allowed to vary in the fit, and is found to be consistent with zero. The *CP* asymmetries of the $B\bar{B}$ backgrounds are expected to be small and so are fixed to zero in the nominal fit. They

TABLE V. Selection criteria imposed to enhance the contributions of signal events for the results presented in Figs. 4 and 5.

Projection plot	Selections
$m_{\rm ES}$	$-0.05 < \Delta E < 0.05$ GeV $\mathrm{BDT_{out}} > 0.1$
ΔE	$m_{\rm ES} > 5.27$ GeV$/c^2$ $\mathrm{BDT_{out}} > 0.1$
$\mathrm{BDT_{out}}$	$m_{\rm ES} > 5.27$ GeV$/c^2$ $-0.05 < \Delta E < 0.05$ GeV
$m_{K^0_S\pi^+}$, $m_{K^0_S\pi^0}$, $m_{\pi^+\pi^0}$	$m_{\rm ES} > 5.27$ GeV$/c^2$ $-0.05 < \Delta E < 0.05$ GeV $\mathrm{BDT_{out}} > 0.1$

TABLE VIII. Measured branching fractions $\mathcal{B}$ from a fit to the combined $B^\pm$ data sample, and CP asymmetries A_{CP} [Eq. (19)]. The first uncertainty is statistical, the second is systematic, and the third is due to the signal model.

Decay channel	$\mathcal{B}(10^{-6})$	A_{CP}
$K^0\pi^+\pi^0$	$31.8 \pm 1.8 \pm 2.1^{+6.0}_{-0.0}$	$0.07 \pm 0.05 \pm 0.03^{+0.02}_{-0.03}$
$K^*(892)^0\pi^+$	$10.1 \pm 1.7 \pm 1.0^{+0.2}_{-0.3}$	$-0.12 \pm 0.21 \pm 0.08^{+0.0}_{-0.11}$
$K^*(892)^+\pi^0$	$6.4 \pm 0.9 \pm 0.4^{+0.2}_{-0.3}$	$-0.52 \pm 0.14 \pm 0.04^{+0.04}_{-0.02}$
$K^*_0(1430)^0\pi^+$	$34.6 \pm 3.3 \pm 4.2^{+1.9}_{-1.8}$	$0.14 \pm 0.10 \pm 0.04^{+0.13}_{-0.05}$
$K^*_0(1430)^+\pi^0$	$11.9 \pm 1.7 \pm 1.0^{+0.0}_{-1.3}$	$0.26 \pm 0.12 \pm 0.08^{+0.12}_{-0.0}$
$\rho(770)^+K^0$	$6.5 \pm 1.1 \pm 0.8^{+0.0}_{-1.7}$	$0.21 \pm 0.19 \pm 0.07^{+0.23}_{-0.19}$

are varied within reasonable ranges based on world average experimental results [28] in order to determine the associated systematic uncertainty.

We find an overall CP asymmetry of $A_{CP}(B^+ \to K^0\pi^+\pi^0) = 0.07 \pm 0.05 \pm 0.03^{+0.02}_{-0.03}$, where the first uncertainty is statistical, the second is systematic, and the third is due to the signal model. This is consistent with zero CP asymmetry. Invariant mass projections for the fit to data allowing for direct CP violation are shown in Fig. 5.

Table VIII shows the results for the branching fractions and CP asymmetries obtained from the fit to data. The first uncertainty is statistical, the second is systematic, and the third is the uncertainty associated with the signal model. We observe a significant asymmetry between the $m_{K^0_S\pi^+}$ and $m_{K^0_S\pi^-}$ distributions in the region of the $K^*(892)^+$ resonance; see Figs. 5(a) and (b). We determine the statistical significance, S, of a nonzero CP asymmetry in $B^+ \to K^*(892)^+\pi^0$ from the difference between the best-fit value of the likelihood, $\mathcal{L}_{A_{CP}}$, and the value when the CP asymmetry is fixed to zero, $\mathcal{L}_0$:

$$S = \sqrt{-2\ln(\mathcal{L}_0/\mathcal{L}_{A_{CP}})}. \tag{29}$$

Using this method, we measure a statistical significance of 3.6 standard deviations for a nonzero A_{CP} in

TABLE VI. Combined $B^\pm$ fit: Relative phases, ϕ, for the isobar amplitudes as measured from five fits to data, where each of the five isobar amplitudes is in turn taken as the reference. All phases are quoted in degrees. The uncertainties are statistical only.

Resonant contribution	Relative phase (degrees)				
Reference amplitude	$K^*(892)^0\pi^+$	$K^*(892)^+\pi^0$	$(K\pi)^{*0}_0\pi^+$	$(K\pi)^{*+}_0\pi^0$	$\rho(770)^+K^0_S$
$B^+ \to K^*(892)^0\pi^+$	0	-95 ± 43	174 ± 11	-89 ± 43	-122 ± 43
$B^+ \to K^*(892)^+\pi^0$	–	0	-90 ± 42	6 ± 10	-27 ± 26
$B^+ \to (K\pi)^{*0}_0\pi^+$	–	–	0	96 ± 42	63 ± 37
$B^+ \to (K\pi)^{*+}_0\pi^0$	–	–	–	0	-32 ± 25
$B^+ \to \rho(770)^+K^0_S$	–	–	–	–	0

TABLE VII. Combined $B^\pm$ fit: Results for the fit fractions FF_j (diagonal terms) and interference terms FF_{ij} in data for each resonant contribution. The uncertainties are statistical only.

	FF_j and FF_{ij}				
Resonant contribution	$K^*(892)^0\pi^+$	$K^*(892)^+\pi^0$	$(K\pi)^{*0}_0\pi^+$	$(K\pi)^{*+}_0\pi^0$	$\rho(770)^+K^0_S$
$B^+ \to K^*(892)^0\pi^+$	0.10 ± 0.03	0.0004 ± 0.0028	$(17 \pm 5) \times 10^{-5}$	0.007 ± 0.005	-0.008 ± 0.007
$B^+ \to K^*(892)^+\pi^0$	–	0.14 ± 0.02	-0.010 ± 0.007	$(-3 \pm 1) \times 10^{-6}$	0.012 ± 0.008
$B^+ \to (K\pi)^{*0}_0\pi^+$	–	–	0.36 ± 0.05	$(1.5 \pm 6.1) \times 10^{-5}$	-0.04 ± 0.02
$B^+ \to (K\pi)^{*+}_0\pi^0$	–	–	–	0.27 ± 0.03	-0.02 ± 0.02
$B^+ \to \rho(770)^+K^0_S$	–	–	–	–	0.19 ± 0.04

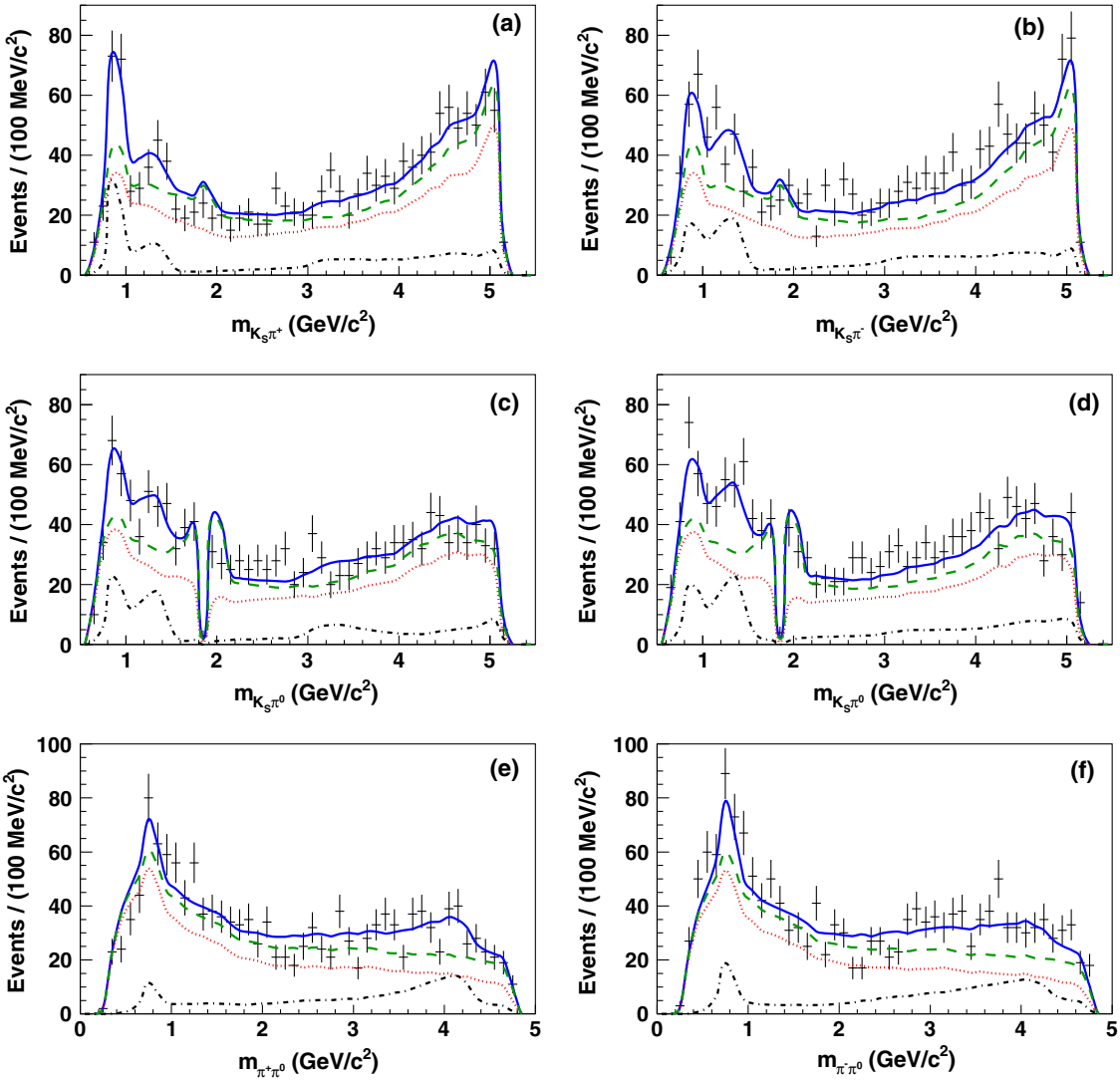

FIG. 5. The *CP* fit: Measured distributions and fit projections for $B^+ \to K^0_S\pi^+\pi^0$ (left column) and $B^- \to K^0_S\pi^-\pi^0$ (right column) candidates; (a) $m_{K^0_S\pi^+}$, (b) $m_{K^0_S\pi^-}$, (c) $m_{K^0_S\pi^0}$ (from $B^+ \to K^0_S\pi^+\pi^0$), (d) $m_{K^0_S\pi^0}$ (from $B^- \to K^0_S\pi^-\pi^0$), (e) $m_{\pi^+\pi^0}$, and (f) $m_{\pi^-\pi^0}$. The points with error bars correspond to data, the solid (blue) curves to the total fit result, the dashed (green) curves to the total background contribution, and the dotted (red) curves to the continuum background component. The dash-dotted curves represent the signal contribution. The projected distributions are obtained from statistically precise pseudo experiments generated using the fit results. For all distributions in each panel, the signal-to-background ratio is increased by applying the tighter selection requirements on $m_{\rm ES}$, ΔE, and/or $\mathrm{BDT_{out}}$, listed in Table V.

$B^+ \to K^*(892)^+\pi^0$. We obtain a consistent result of 3.7 standard deviations for the statistical significance by dividing the central value of the *CP* asymmetry by the statistical uncertainty, indicating that the log-likelihood function is close to parabolic. Figure 6 displays the contours in the complex plane of the coefficients $c = (x + \Delta x, y + \Delta y)$, defined in Eq. (4), for $B^+ \to K^*(892)^+\pi^0$ decays, and of $\bar{c} = (x - \Delta x, y - \Delta y)$, defined in Eq. (5), for $B^- \to K^*(892)^-\pi^0$ decays. For other resonances the *CP* asymmetry is within 2 standard deviations of zero.

We also express the complex isobar coefficients c and $\bar{c}$ of Eq. (18) in terms of amplitudes and phases,

$$c = A_+ e^{i\phi_+}, \tag{30}$$

$$\bar{c} = A_- e^{-i\phi_-}. \tag{31}$$

Table IX presents the results, measured with respect to the $B^\pm \to K^*(892)^0\pi^\pm$ reference amplitude. The statistical uncertainties of the separate B^+ and B^- decay amplitudes,

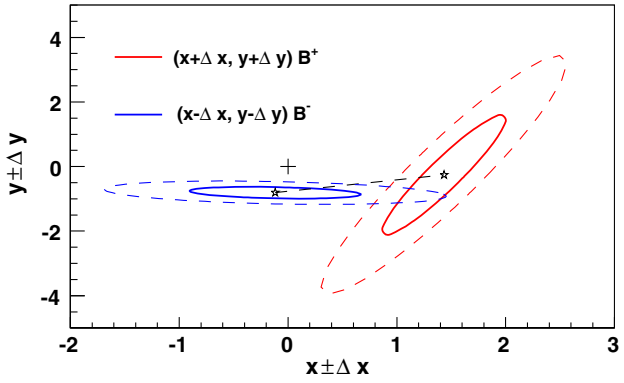

FIG. 6. *CP* parameters $(x \pm \Delta x, y \pm \Delta y)$ obtained from the fit to data for $B^{\pm} \to K^{*\pm}(892)\pi^0$ resonant decay including the 1 and 2 standard deviation contours (solid and dashed curves). The contours are estimated by calculating the uncertainty and correlation between the two *CP* parameters. The stars indicate the central values of the *CP* parameters and the cross sign the origin of the plot.

A_+ and A_-, vary between 0.1 and 0.3. We thus obtain significant statistical precision for these terms. With respect to the phases, ϕ_+ and ϕ_-, only the $(K\pi)_0^{*0}\pi^+$ amplitude yields a statistically precise result. For the other amplitudes, the statistical uncertainty ranges between 70° and 170°, and only the statistical uncertainty is quoted. For the more precisely determined variables, systematic uncertainties are evaluated as well. Because the statistical uncertainties on the phases of the $(K\pi)_0^{*\pm}\pi^0$ and $K^*(892)^{\pm}\pi^0$ amplitudes listed in Table IX are highly correlated, we also calculate the phase differences, for which the statistical uncertainties are smaller. The results, including systematic uncertainties, are:

$$\phi_+((K\pi)_0^{*+}\pi^0) - \phi_+(K^*(892)^+\pi^0) = (-14 \pm 18 \pm 9^{+4}_{-3})^\circ,$$
$$\phi_-((K\pi)_0^{*-}\pi^0) - \phi_-(K^*(892)^-\pi^0) = (11 \pm 19 \pm 10^{+17}_{-9})^\circ. \quad (32)$$

TABLE X. Combined *BABAR* measurements of branching fractions and *CP* asymmetries of $B^+ \to K^*(892)^0\pi^+$ and $B^+ \to K^*{}_0(1430)^0\pi^+$ from $B^+ \to K^0_S\pi^+\pi^0$ (this analysis) and $B^+ \to K^+\pi^-\pi^+$ [16], and of $B^+ \to K^*(892)^+\pi^0$ from $B^+ \to K^0_S\pi^+\pi^0$ and $B^+ \to K^+\pi^0\pi^0$ [18]. The first uncertainty is statistical and the second is systematic.

Decay channel	$\mathcal{B}(10^{-6})$	A_{CP}
$K^*(892)^0\pi^+$	$10.5 \pm 0.6 \pm 0.9$	$0.025 \pm 0.050 \pm 0.016$
$K^*(892)^+\pi^0$	$6.8 \pm 0.8 \pm 0.5$	$-0.39 \pm 0.12 \pm 0.03$
$K^*{}_0(1430)^0\pi^+$	$34.1 \pm 1.1 \pm 4.3$	$0.040 \pm 0.033 \pm 0.033$

VIII. SYSTEMATIC UNCERTAINTIES

We evaluate systematic uncertainties to account for effects that could affect the branching fractions, phases, and asymmetries, by varying the fixed parameters. The systematic uncertainties described in this section are summarized in Tables XI through XVI of Appendix A.

The uncertainties associated with the branching fractions are listed in Table XI. To estimate the uncertainty related to the modeling of the SCF PDFs, we implement a simpler model consisting of only four regions in the Dalitz plot. The PDFs are defined by the distribution of SCF MC events in each of these new regions. We then fit the data using the new SCF model and take the uncertainties to be the change in the fit parameters compared to those obtained from the nominal fit to data. All relative systematic uncertainties due to the SCF $m_{\rm ES}$ and ΔE PDFs range from approximately 1% to 4%, except for the relative systematic uncertainty for the $B^+ \to \rho(770)^+K^0$ decay, which is 7.5%. This is consistent with expectations from simulation that more than half the $B^+ \to \rho(770)^+K^0$ events are due to SCF.

The uncertainties associated with the number of $B\bar{B}$ background events are evaluated by varying the estimates within their uncertainties, which are primarily due to uncertainties in the branching fractions. The uncertainties related to the $B\bar{B}$ background $m_{\rm ES}$, ΔE, and $\mathrm{BDT}_{\rm out}$ PDFs are accounted for by varying the histogram bin contents

TABLE IX. Results for the relative phases ϕ obtained from the combined $B^{\pm}$ fit, the *CP* amplitudes A_+ and A_-, and the *CP* phases ϕ_+ and ϕ_- obtained from the *CP* fit. All parameters are measured relative to the $B^{\pm} \to K^*(892)^0\pi^{\pm}$ reference amplitude. The first uncertainty is statistical, the second is systematic, and the third is due to the signal model. Note that for the *CP* phases of all contributions except for $B^{\pm} \to (K\pi)_0^{*0}\pi^{\pm}$, only statistical uncertainties are quoted.

Isobar	ϕ (°)	A_+	A_-	ϕ_+ (°)	ϕ_- (°)
$K^*(892)^{\pm}\pi^0$	$-95 \pm 43^{+48+8}_{-36-70}$	$1.46 \pm 0.22 \pm 0.05^{+0.05}_{-0.03}$	$0.82 \pm 0.18 \pm 0.05^{+0.06}_{-0.04}$	-10 ± 112	-98 ± 97
$(K\pi)_0^{*0}\pi^{\pm}$	$174 \pm 11 \pm 11^{+0}_{-6}$	$1.74 \pm 0.21 \pm 0.11^{+0.07}_{-0.12}$	$2.00 \pm 0.27 \pm 0.13^{+0.14}_{-0.02}$	$165 \pm 19 \pm 9^{+4}_{-3}$	$190 \pm 21 \pm 11^{+1}_{-3}$
$(K\pi)_0^{*\pm}\pi^0$	$-89 \pm 43^{+53+5}_{-40-17}$	$1.44 \pm 0.22 \pm 0.13^{+0.00}_{-0.10}$	$1.88 \pm 0.25 \pm 0.14^{+0.22}_{-0.06}$	4 ± 111	-109 ± 92
$\rho(770)^{\pm}K^0$	$-122 \pm 43^{+55+16}_{-47-66}$	$1.24 \pm 0.01 \pm 0.09^{+0.00}_{-0.21}$	$1.54 \pm 0.01 \pm 0.09^{+0.23}_{-0.09}$	-50 ± 168	-120 ± 71

according to their statistical uncertainties. The uncertainty is then taken as the RMS of the distribution of the difference in the fit parameters. The uncertainties related to the limited statistical precision of the MC and data-sideband samples are similarly accounted for by varying the results in the corresponding histogram bins by their uncertainties. The uncertainty due to possible variations of the SCF fraction is estimated by varying each bin of the PDF distribution by an uncertainty of 2%.

The uncertainty in the $\mathrm{BDT_{out}}$ histogram PDFs for correctly reconstructed and SCF signal events is determined by varying the bin contents in accordance with the observed data/MC difference. For correctly reconstructed signal events, the tails of the asymmetric Gaussian PDFs for m_{ES} and ΔE are fixed. To account for an associated uncertainty, we allow the relevant parameters to vary in a fit to data and use the variation in the fit parameters to define the uncertainty.

To validate the fitting procedure, 500 MC pseudo experiments are generated, using the PDFs with parameter values found from the fit to data. Small fit biases are found for some of the fit parameters and are included in the systematic uncertainties.

We also account for uncertainties in the following parameters describing the signal model: the mass and width of each resonance and the value of the Blatt-Weisskopf barrier radius. The associated uncertainties are determined by varying the parameters within their uncertainties (some of which are given in Table II) and refitting.

The uncertainties in the branching fractions related to particle identification, tracking efficiency, and the total number of $B\bar{B}$ events are 1.0%, 1.0%, and 0.6%, respectively. We estimate systematic uncertainties in the branching fractions associated with the π^0 and K^0_S reconstruction efficiencies to be 1.0% and 1.1%, respectively.

Uncertainties from all the above sources are added in quadrature to yield the total systematic uncertainties, which are listed in Table XI.

We determine changes in the branching fractions, $\Delta\mathcal{B}$, when the signal model is varied. The systematic uncertainties in the branching fractions due to the $(K\pi)_0^{*0/+}$ parametrization are estimated by replacing the LASS model with another phenomenologically inspired parametrization [47]. We take the differences in branching fractions with respect to the nominal fit as the systematic uncertainty. This is the largest contribution to the uncertainty due to the model. Another uncertainty reflects any changes in the fit parameters for the nominal model when including components that are omitted in the nominal fit, such as the $\rho(1450)^+$, $K^*{}_2(1430)^0$, $K^*{}_2(1430)^+$, $K^*(1680)^0$, and $K^*(1680)^+$. Positive and negative variations are added separately in quadrature to obtain the systematic uncertainties due to the signal model, listed in Table XI.

We determine systematic uncertainties in the phases averaged over B^+ and B^- decays from the same sources as considered for the branching fractions. The variations in the phases are measured relative to the $K^*(892)^0\pi^+$ amplitude. Since the differences between positive and negative shifts in the phases, shown in Table XII, are large in some cases, we quote for those phase shifts asymmetric systematic uncertainties.

Reconstruction and particle identification efficiencies cancel to first order in the fit to *CP* asymmetries; therefore the only uncertainties that are included for A_{CP} are those coming from the fit and signal model. In addition to this, we do not evaluate any of the uncertainties that are found to be negligible for the branching fractions.

An additional uncertainty for A_{CP} arises from having fixed the *CP* asymmetries for individual $B\bar{B}$ background components to zero. We vary the *CP* asymmetry individually for each B background category, based on the world-average experimental results [9], and take as the corresponding uncertainty the sum in quadrature of the largest of the positive or negative change in A_{CP}.

The uncertainty related to the efficiency model is determined by exchanging the efficiency maps for the positive and negative Dalitz plots and refitting the data. We then take the difference in *CP* asymmetry with respect to the nominal fit as the uncertainty.

We list in Table XIII the systematic uncertainties associated with the signal *CP* asymmetries and the variations in the asymmetry due to changes in the signal composition.

We evaluate systematic uncertainties for the *CP* amplitudes and *CP* phases from the same sources as for the *CP* asymmetries. We list the variations to the amplitudes A_+ in Table XIV and to the amplitudes A_- in Table XV, including the uncertainties due to changes to the signal model. Table XVI lists the systematic variations and model uncertainties for $\phi_{+(-)}((K\pi)_0^{*0}\pi^{+(-)} - K^*(892)^0\pi^{+(-)})$ and $\phi_{+(-)}((K\pi)_0^{*+(-)}\pi^0 - K^*(892)^{+(-)}\pi^0)$.

IX. SUMMARY AND CONCLUSIONS

The measured branching fractions and *CP* asymmetries are summarized in Table VIII, and the amplitude and phase values in Table IX, including statistical, systematic, and model uncertainties. We have measured for the first time the branching fraction and *CP* asymmetry for the decay $B^+ \to K^0\pi^+\pi^0$. We obtain first evidence for direct *CP* violation in the intermediate decay $B^+ \to K^*(892)^+\pi^0$, with a total significance of 3.4 standard deviations determined by adding statistical, systematic, and signal-model uncertainties in quadrature and dividing the measured A_{CP} by the total uncertainty.

In addition, we have measured the branching fractions, *CP* asymmetries, and relative *CP*-averaged phase values

of the decays $B^+ \to K^*(892)^0\pi^+$, $B^+ \to K^*(892)^+\pi^0$, $B^+ \to K^*_0(1430)^0\pi^+$, $B^+ \to K^*_0(1430)^+\pi^0$, and $B^+ \to \rho(770)^+K^0$. The results for the branching fractions and CP asymmetries for $B^+ \to K^*(892)^0\pi^+$ are consistent with the previous measurements from $B^+ \to K^+\pi^-\pi^+$ decays by the Belle and *BABAR* Collaborations and the branching fraction for $B^+ \to K^*_0(1430)^0\pi^+$ is consistent with the previous *BABAR* measurement and within two standard deviations of the Belle measurement [16,17]. The branching fraction for $B^+ \to K^*(892)^+\pi^0$ is consistent with the previous measurement from the *BABAR* Collaboration in the $B^+ \to K^+\pi^0\pi^0$ decay mode and the result for A_{CP} is within two standard deviations of the previous measurement [18]. The branching fraction and A_{CP} results for $B^+ \to \rho(770)^+K^0$ supersede the previous *BABAR* measurements [14]. The CP asymmetries of $B^+ \to K^*(892)^0\pi^+$, $B^+ \to K^*_0(1430)^0\pi^+$, and $B^+ \to \rho(770)^+K^0$ are all consistent with zero, as expected. We obtain the first measurements of the branching fraction and CP asymmetry for $B^+ \to K^*_0(1430)^+\pi^0$, with a significance of 5.4 standard deviations for the branching fraction.

We combine our results for the branching fractions and CP asymmetries of $B^+ \to K^*(892)^0\pi^+$, $B^+ \to K^*_0(1430)^0\pi^+$, and $B^+ \to K^*(892)^+\pi^0$ with the previous *BABAR* measurements. The statistical uncertainties and all systematic uncertainties for the CP asymmetries are uncorrelated between the measurements. For the branching fractions, we account for possible correlations when combining the systematic uncertainties. If the systematic uncertainties are asymmetric, the average systematic uncertainty is calculated from the largest limit. The combined results from *BABAR* for these decay modes are presented in Table X.

Using the world average value for direct CP violation in $B^0 \to K^*(892)^+\pi^-$ [9] and the final *BABAR* result for direct CP violation in $B^+ \to K^*(892)^+\pi^0$, we calculate ΔA_{CP} for the $K^*\pi$ system to be

$$\begin{aligned}\Delta A_{CP}(K^*\pi) &= A_{CP}(K^{*+}\pi^0) - A_{CP}(K^{*+}\pi^-) \\ &= -0.16 \pm 0.13. \end{aligned} \tag{33}$$

Thus the value of ΔA_{CP} in $K^*\pi$ is found to be consistent with zero. The uncertainty in the $\Delta A_{CP}(K^*\pi)$ result remains large, rendering the comparison to $\Delta A_{CP}(K\pi)$, given in Eq. (3), inconclusive at present and motivating improved determinations in future experiments.

ACKNOWLEDGMENTS

We are grateful for the extraordinary contributions of our PEP-II colleagues in achieving the excellent luminosity and machine conditions that have made this work possible. The success of this project also relies critically on the expertise and dedication of the computing organizations that support *BABAR*. The collaborating institutions wish to thank SLAC for its support and the kind hospitality extended to them. This work is supported by the US Department of Energy and National Science Foundation, the Natural Sciences and Engineering Research Council (Canada), the Commissariat à l'Energie Atomique and Institut National de Physique Nucléaire et de Physique des Particules (France), the Bundesministerium für Bildung und Forschung and Deutsche Forschungsgemeinschaft (Germany), the Istituto Nazionale di Fisica Nucleare (Italy), the Foundation for Fundamental Research on Matter (The Netherlands), the Research Council of Norway, the Ministry of Education and Science of the Russian Federation, Ministerio de Economía y Competitividad (Spain), the Science and Technology Facilities Council (United Kingdom), and the Binational Science Foundation (U.S.-Israel). Individuals have received support from the Marie-Curie IEF program (European Union) and the A. P. Sloan Foundation (USA).

APPENDIX: TABLES OF SYSTEMATIC AND MODEL UNCERTAINTIES

Table XI lists the uncertainties in the branching fractions due to systematic effects, efficiency corrections, and changes to the signal model. Table XII lists uncertainties in the relative phase values (for B^+ and B^- decays combined) due to systematic effects and changes to the signal model. Tables XIII, XIV, XV, and XVI list the systematic and signal model uncertainties for the CP asymmetries, the amplitudes for the B^+ and B^- Dalitz plots, A_+ and A_-, respectively, and the corresponding phases ϕ_+ and ϕ_- for the $B^+ \to K^*_0(1430)^0\pi^+$ amplitude relative to that for $B^+ \to K^*(892)^0\pi^+$, and the phase values for the $B^+ \to (K\pi)^{*+}_0\pi^0$ amplitude relative to that for $B^+ \to K^*(892)^+\pi^0$.

TABLE XI. Combined $B^{\pm}$ fit: Systematic uncertainties for the branching fraction measurements, including uncertainties due to the signal model. For each of the four alternative signal models (described in the text), we give the change in the branching fraction; positive and negative changes are added separately in quadrature to obtain the total positive $(+)$ and negative $(-)$ uncertainties listed in the last two rows.

Resonant contribution	Relative Variations of branching fraction (%)					
Source	Inclusive	$K^*(892)^0$	$K^*(892)^+$	$K^*{}_0(1430)^0$	$K^*{}_0(1430)^+$	$\rho(770)^+$
Correctly reconstructed $m_{\rm ES}$ and ΔE PDF (fixed parameters)	0.8	1.1	0.6	1.1	0.7	1.2
Correctly reconstructed and self cross feed signal $\mathrm{BDT_{out}}$ PDFs	3.3	3.3	3.4	3.4	4.2	4.0
Self cross feed signal $m_{\rm ES}$ and ΔE PDF models	3.0	4.3	3.1	1.3	1.8	7.5
Fit bias	0.3	0.9	0.6	0.5	0.7	0.9
$B\bar{B}$ background $m_{\rm ES}$, ΔE and $\mathrm{BDT_{out}}$ PDFs	0.3	0.4	0.2	0.3	0.5	0.6
$B\bar{B}$ background yields	0.7	1.2	0.6	0.9	2.0	1.8
Background model in Dalitz plot	1.5	3.7	2.8	2.8	2.7	3.5
Signal efficiency model	0.3	1.8	1.0	0.4	0.4	0.8
Self cross feed PDF model	0.3	0.4	0.6	0.3	0.3	0.5
$K^*(892)$ mass and width	0.1	0.7	0.3	0.1	0.2	0.1
$K_0^*(1430)$ mass and width	3.2	3.8	2.1	8.1	5.5	4.0
$\rho(770)^+$ mass and width	<0.1	0.2	0.1	0.1	0.2	0.3
Blatt-Weisskopf radius	2.3	4.4	2.9	7.4	2.9	3.7
Subtotal	6.3	9.1	6.7	12.0	8.5	11.0
Neutral pion efficiency	1.0	1.0	1.0	1.0	1.0	1.0
K_S^0 efficiency	1.1	1.1	1.1	1.1	1.1	1.1
Charged particle identification efficiency	1.0	1.0	1.0	1.0	1.0	1.0
Tracking efficiency	1.0	1.0	1.0	1.0	1.0	1.0
$N_{B\bar{B}}$	0.6	0.6	0.6	0.6	0.6	0.6
Total	6.6	9.4	7.0	12.2	8.7	11.2
Changes due to signal model				$\Delta\mathcal{B}(10^{-6})$		
$(K\pi)_0^{*0}/(K\pi)_0^{*+}$ parametrization	$+5.5$	-0.2	-0.2	–	–	-0.9
$\rho(1450)^+$	$+1.6$	$+0.2$	-0.3	$+1.8$	-0.6	-1.4
$K^*{}_2(1430)^0$ and $K^*{}_2(1430)^+$	$+1.0$	-0.2	$+0.2$	-1.8	-0.6	-0.2
$K^*(1680)^0$ and $K^*(1680)^+$	$+1.2$	–	–	$+0.4$	-1.0	-0.2
Total $(+)$	$+6.0$	$+0.2$	$+0.2$	$+1.9$	$+0.0$	$+0.0$
Total $(-)$	-0.0	-0.3	-0.3	-1.8	-1.3	-1.7

TABLE XII. Combined $B^{\pm}$ fit: Systematic uncertainties due to the fit model and the fixed shapes in the parametrization (top part of table), and changes to the signal model (bottom part of table), for the relative phases (in degrees) measured relative to the $K^*(892)^0\pi^+$ amplitude. For each of the four alternative signal models (described in the text), we give the change in the branching fraction; positive and negative changes are added separately in quadrature to obtain the total positive (+) and negative (−) uncertainties listed in the last two rows.

Resonant contribution	Systematic Variations (°)			
Systematic	$K^*(892)^+\pi^0$	$K^*{}_0(1430)^0\pi^+$	$K^*{}_0(1430)^+\pi^0$	$\rho(770)^+K^0_S$
Self cross feed PDFs and mapping	7.4	1.4	9.6	6.7
Correctly reconstructed and self cross feed $\mathrm{BDT_{out}}$ PDFs	1.4	0.9	1.3	1.3
$B\bar{B}$ background yields	1.7	0.5	1.8	2.1
Correctly reconstructed m_{ES} and ΔE PDF	0.4	0.2	0.9	1.2
Background DP PDF	5.7	2.2	4.5	5.4
$B\bar{B}$ background m_{ES}, ΔE, $\mathrm{BDT_{out}}$ PDFs	0.3	0.2	0.3	0.3
Signal efficiency model	0.5	0.4	0.7	0.7
Fit bias	9.3	7.8	7.3	23.5
$K^*(892)$ mass	1.4	0.2	1.2	1.4
$K^*(892)$ width	0.3	0.1	0.1	<0.1
$K^*_0(1430)$ mass	$^{+43}_{-33}$	$^{+5.2}_{-4.7}$	$^{+48}_{-37}$	$^{+46}_{-36}$
$K^*_0(1430)$ width	5.2	4.0	5.7	14.6
$\rho(770)^+$ mass	0.3	0.1	0.4	1.0
$\rho(770)^+$ width	0.6	0.1	0.6	0.2
Blatt-Weisskopf radius	$^{+15}_{-2}$	$^{+1.0}_{-1.4}$	$^{+17}_{-3}$	$^{+0.3}_{-0.5}$
Total	$^{+48}_{-36}$	$^{+11}_{-11}$	$^{+53}_{-40}$	$^{+55}_{-47}$
	Changes due to signal model			
$(K\pi)^{*0}_0/(K\pi)^{*+}_0$ parametrization	−67.0	–	–	−60.3
$\rho(1450)^+$	−18.4	−2.8	−11.8	−27.4
$K^*_2(1430)$	+7.8	−3.1	+5.5	+11.3
$K^*(1680)$	−7.8	−4.9	−12.9	+11.8
Total (+)	+7.8	+0.0	+5.5	+16.4
Total (−)	−69.9	−6.5	−17.5	−66.2

TABLE XIII. Contributions to the uncertainties in the *CP* asymmetries for the overall and resonant isobar contributions, including uncertainties due to changes to the signal model. For each of the four alternative signal models (described in the text), we give the change in the branching fraction; positive and negative changes are added separately in quadrature to obtain the total positive (+) and negative (−) uncertainties listed in the last two rows.

Resonant contribution	Systematic Variations of A_{CP} (%)					
Systematic	Inclusive	$K^*(892)^0\pi^+$	$K^*(892)^+\pi^0$	$K^*{}_0(1430)^0\pi^+$	$K^*{}_0(1430)^+\pi^0$	$\rho(770)^+K^0_S$
Self cross feed PDFs and mapping	2.0	6.0	1.0	1.2	0.9	5.0
Correctly reconstructed and self cross feed $\mathrm{BDT_{out}}$ PDFs	0.7	1.7	1.8	1.6	1.1	2.8
$B\bar{B}$ background asymmetries	2.5	1.4	1.7	1.8	7.5	2.3
Background DP PDF	0.7	2.7	2.1	2.8	2.0	2.5
$B\bar{B}$ background m_{ES}, ΔE, $\mathrm{BDT_{out}}$ PDFs	0.2	0.1	0.2	0.3	0.5	0.4
Signal efficiency model	0.2	3.9	2.1	0.1	0.9	1.3
Fit bias	0.3	1.4	0.8	1.9	1.0	1.2
$K^*(892)$ mass and width	0.1	0.2	0.4	0.2	0.2	0.2
$K^*_0(1430)$ mass and width	1.1	4.4	0.5	3.0	2.8	2.2
$\rho(770)^+$ mass and width	<0.1	0.1	0.1	0.2	0.1	0.1
Blatt-Weisskopf radius	<0.1	0.9	0.3	0.8	1.1	0.5
Total	3.4	8.1	4.1	4.3	8.0	6.9
	Changes due to signal model					
$(K\pi)^{*0}_0/(K\pi)^{*+}_0$ parametrization	−0.7	+6.2	+2.0	–	–	−8.1
$\rho(1450)^+$	+3.3	+1.5	−3.4	−10.5	−11.6	−21.3
$K^*_2(1430)$	−0.2	+5.7	−1.5	−7.5	−2.7	+14.4
$K^*(1680)$	−2.2	+6.3	+0.5	+4.8	−1.9	+12.3
Total (+)	+2.4	+0.0	+3.7	+13.0	+12.0	+22.8
Total (−)	−3.3	−10.6	−2.0	−4.8	−0.0	−19.0

TABLE XIV. Variations in the *CP* amplitude, A_+, including uncertainties due to changes to the signal model (bottom part of table). In the fits, the amplitudes are measured relative to the $K^*(892)^0\pi^+$ amplitude. For each of the four alternative signal models (described in the text), we give the change in the branching fraction; positive and negative changes are added separately in quadrature to obtain the total positive (+) and negative (−) uncertainties listed in the last two rows.

Resonant contribution	Variation of A_+			
Systematic	$K^*(892)^+\pi^0$	$(K\pi)_0^{*0}\pi^+$	$(K\pi)_0^{*+}\pi^0$	$\rho(770)^+K_S^0$
Self cross feed PDFs and mapping	0.02	0.02	0.04	0.02
Correctly reconstructed and self cross feed $\mathrm{BDT_{out}}$ PDFs	0.01	0.03	0.02	0.02
$B\bar{B}$ background asymmetries	0.01	0.03	0.07	0.02
Background DP PDF	0.02	0.06	0.04	0.04
$B\bar{B}$ background m_{ES}, ΔE, $\mathrm{BDT_{out}}$ PDFs	<0.01	0.01	0.01	<0.01
Signal efficiency model	0.01	0.01	<0.01	0.01
Fit bias	0.01	0.03	0.02	0.03
$K^*(892)$ mass	0.01	0.01	0.01	<0.01
$K^*(892)$ width	<0.01	0.01	0.01	<0.1
$(K\pi)_0^*$ mass	0.02	0.02	0.09	0.06
$(K\pi)_0^*$ width	0.02	0.06	0.01	0.02
$\rho(770)^+$ mass	<0.01	<0.01	<0.01	<0.01
$\rho(770)^+$ width	<0.01	<0.01	<0.01	<0.01
Blatt-Weisskopf radius	0.02	0.03	0.02	0.02
Total	0.05	0.11	0.13	0.09
	Changes due to signal model			
$(K\pi)_0^{*0}/(K\pi)_0^{*+}$ parametrization	−0.03	−−	−−	−0.17
$\rho(1450)^+$	<0.01	−0.01	−0.02	−0.12
$K_2^*(1430)$	0.05	−0.08	−0.08	−0.04
$K^*(1680)$	−0.02	0.07	−0.05	−0.05
Total (+)	+0.05	+0.07	+0.00	+0.00
Total (−)	−0.03	−0.12	−0.10	−0.21

TABLE XV. Variations in the *CP* amplitude, A_-, including uncertainties due to changes to the signal model (bottom part of table). In the fits, the amplitudes are measured relative to the $K^*(892)^0\pi^+$ amplitude. For each of the four alternative signal models (described in the text), we give the change in the branching fraction; positive and negative changes are added separately in quadrature to obtain the total positive (+) and negative (−) uncertainties listed in the last two rows.

Resonant contribution	Variation of A_-			
Systematic	$K^*(892)^-\pi^0$	$(K\pi)_0^{*0}\pi^-$	$(K\pi)_0^{*-}\pi^0$	$\rho(770)^-K_S^0$
Self cross feed PDFs and mapping	<0.01	0.05	0.04	0.05
Correctly reconstructed and self cross feed $\mathrm{BDT_{out}}$ PDFs	0.02	0.02	0.02	0.03
$B\bar{B}$ background asymmetries	0.01	0.01	0.06	0.02
Background DP PDF	0.02	0.05	0.04	0.03
$B\bar{B}$ background m_{ES}, ΔE, $\mathrm{BDT_{out}}$ PDFs	<0.01	<0.01	<0.01	<0.01
Signal efficiency model	0.02	<0.01	0.02	0.02
Fit bias	0.02	<0.01	0.02	0.02
$K^*(892)$ mass	<0.01	0.01	0.01	<0.01
$K^*(892)$ width	<0.01	0.01	0.01	0.01
$(K\pi)_0^*$ mass	0.01	0.08	0.08	0.04
$(K\pi)_0^*$ width	0.01	0.07	0.05	0.03
$\rho(770)^+$ mass	<0.01	<0.01	<0.01	<0.01
$\rho(770)^+$ width	<0.01	<0.01	<0.01	<0.01
Blatt-Weisskopf radius	0.01	0.01	0.05	0.01
Total	0.05	0.13	0.14	0.09
	Changes due to signal model			
$(K\pi)_0^{*0}/(K\pi)_0^{*+}$ parametrization	−0.04	−−	−−	−0.09
$\rho(1450)^+$	0.04	0.12	0.22	0.22
$K_2^*(1430)$	0.05	0.07	0.05	0.03
$K^*(1680)$	−0.01	−0.02	−0.02	−0.04
Total (+)	+0.06	+0.14	+0.22	+0.23
Total (−)	−0.04	−0.02	−0.06	−0.09

TABLE XVI. Variations in the *CP* phase values $\phi_\pm$ (in degrees) measured for the $(K\pi)_0^{*0}\pi^\pm$ amplitude relative to the $K^*(892)^0\pi^\pm$ amplitude, and for the $(K\pi)_0^{*\pm}\pi^0$ amplitude relative to the $K^*(892)^\pm\pi^0$ amplitude. For each of the four alternative signal models (described in the text), we give the change in the branching fraction; positive and negative changes are added separately in quadrature to obtain the total positive (+) and negative (−) uncertainties listed in the last two rows.

	Absolute variations of *CP* phase values			
	$(K\pi)_0^{*0}\pi^\pm - K^*(892)^0\pi^\pm$		$(K\pi)_0^{*\pm}\pi^0 - K^*(892)^\pm\pi^0$	
Systematic	ϕ_+	ϕ_-	ϕ_+	ϕ_-
Self cross feed PDFs and mapping	0.6	4.5	1.6	3.1
Correctly reconstructed and self cross feed $\mathrm{BDT_{out}}$ PDFs	0.9	1.6	1.4	2.6
$B\bar{B}$ background asymmetries	1.4	1.3	0.7	1.0
Background DP PDF	2.5	3.0	2.0	2.7
$B\bar{B}$ background m_{ES}, ΔE, $\mathrm{BDT_{out}}$ PDFs	0.2	0.2	0.2	0.4
Signal efficiency model	0.3	1.4	0.8	1.2
Fit bias	2.4	5.2	1.7	0.9
$K^*(892)$ mass	0.2	0.2	0.4	0.6
$K^*(892)$ width	0.3	0.3	0.2	0.2
$(K\pi)_0^*$ mass	6.1	5.3	5.9	5.5
$(K\pi)_0^*$ width	4.2	5.0	5.2	4.5
$\rho(770)^+$ mass	0.2	0.2	<0.1	0.2
$\rho(770)^+$ width	0.2	0.2	0.1	0.2
Blatt-Weisskopf radius	1.0	3.3	1.3	3.8
Total	8.5	11.3	8.7	9.6
	Changes due to signal model			
$\rho(1450)^+$	+3.7	−0.9	−3.2	+9.4
$K_2^*(1430)$	−2.6	+0.5	+3.6	−8.8
$K^*(1680)$	+1.9	+3.3	+2.2	+14.6
Total (+)	+4.2	+0.5	+4.2	+17.4
Total (−)	−2.6	−3.4	−3.2	−8.8

[1] N. Cabibbo, Phys. Rev. Lett. **10**, 531 (1963).
[2] M. Kobayashi and T. Maskawa, Prog. Theor. Phys. **49**, 652 (1973).
[3] M. Ciuchini, M. Pierini, and L. Silvestrini, Phys. Rev. D **74**, 051301 (2006).
[4] M. Gronau, D. Pirjol, A. Soni, and J. Zupan, Phys. Rev. D **75**, 014002 (2007).
[5] B. Aubert *et al.* (*BABAR* Collaboration), Phys. Rev. D **76**, 091102 (2007).
[6] S. W. Lin *et al.* (Belle Collaboration), Nature (London) **452**, 332 (2008).
[7] M. Gronau, Phys. Lett. B **627**, 82 (2005).
[8] A. J. Buras, R. Fleischer, S. Recksiegel, and F. Schwab, Phys. Rev. Lett. **92**, 101804 (2004).
[9] Y. Amhis *et al.* (Heavy Flavor Averaging Group Collaboration), arXiv:1207.1158.
[10] M. Gronau and J. L. Rosner, Phys. Lett. B **666**, 467 (2008).
[11] Q. Chang, X.-Q. Li, and Y.-D. Yang, J. High Energy Phys. 09 (2008) 038.
[12] C.-W. Chiang and D. London, Mod. Phys. Lett. A **24**, 1983 (2009).
[13] M. Gronau, D. Pirjol, and J. Zupan, Phys. Rev. D **81**, 094011 (2010).
[14] B. Aubert *et al.* (*BABAR* Collaboration), Phys. Rev. D **76**, 011103 (2007).
[15] E. Eckhart *et al.* (CLEO Collaboration), Phys. Rev. Lett. **89**, 251801 (2002).
[16] B. Aubert *et al.* (*BABAR* Collaboration), Phys. Rev. D **78**, 012004 (2008).
[17] A. Garmash *et al.* (Belle Collaboration), Phys. Rev. Lett. **96**, 251803 (2006).
[18] J. P. Lees *et al.* (*BABAR* Collaboration), Phys. Rev. D **84**, 092007 (2011).
[19] J. P. Lees *et al.* (*BABAR* Collaboration), Phys. Rev. D **83**, 112010 (2011).
[20] B. Aubert *et al.* (*BABAR* Collaboration), Phys. Rev. D **80**, 112001 (2009).
[21] J. Dalseno *et al.* (Belle Collaboration), Phys. Rev. D **79**, 072004 (2009).

[22] A. Garmash *et al.* (Belle Collaboration), Phys. Rev. D **75**, 012006 (2007).
[23] P. Chang *et al.* (Belle Collaboration), Phys. Lett. B **599**, 148 (2004).
[24] T. Latham, J. Back, and P. Harrison, `Laura++`, http://laura.hepforge.org.
[25] G. N. Fleming, Phys. Rev. **135**, B551 (1964).
[26] D. Herndon, P. Soding, and R. Cashmore, Phys. Rev. D **11**, 3165 (1975).
[27] J. Blatt and V. Weisskopf, *Theoretical Nuclear Physics* (J. Wiley and Sons, New York, 1952).
[28] J. Beringer *et al.* (Particle Data Group Collaboration), Phys. Rev. D **86**, 010001 (2012).
[29] C. Zemach, Phys. Rev. **140**, B109 (1965).
[30] A. Bevan, B. Golob, T. Mannel, S. Prell, and B. Yabsley (*BABAR* Collaboration, Belle Collaboration), Eur. Phys. J. C **74**, 3026 (2014).
[31] R. Barate *et al.* (ALEPH Collaboration), Z. Phys. C **76**, 15 (1997).
[32] R. Akhmetshin *et al.* (CMD-2 Collaboration), Phys. Lett. B **527**, 161 (2002).
[33] D. Aston *et al.* (LASS Collaboration), Nucl. Phys. **B296**, 493 (1988).
[34] G. Gounaris and J. Sakurai, Phys. Rev. Lett. **21**, 244 (1968).
[35] J. P. Lees *et al.* (*BABAR* Collaboration), Nucl. Instrum. Methods Phys. Res., Sect. A **726**, 203 (2013).
[36] B. Aubert *et al.* (*BABAR* Collaboration), Nucl. Instrum. Methods Phys. Res., Sect. A **479**, 1 (2002).
[37] B. Aubert *et al.* (*BABAR* Collaboration), Nucl. Instrum. Methods Phys. Res., Sect. A **729**, 615 (2013).
[38] S. Agostinelli *et al.* (GEANT4 Collaboration), Nucl. Instrum. Methods Phys. Res., Sect. A **506**, 250 (2003).
[39] J. Allison *et al.*, IEEE Trans. Nucl. Sci. **53**, 270 (2006).
[40] A. Ryd *et al.*, Report No. EVTGEN-V00-11-07, 2005.
[41] T. Sjöstrand, Comput. Phys. Commun. **82**, 74 (1994).
[42] A. Drescher, B. Gräwe, B. Hahn, B. Ingelbach, U. Matthiesen, H. Scheck, J. Spengler, and D. Wegener, Nucl. Instrum. Methods Phys. Res., Sect. A **237**, 464 (1985).
[43] B. Aubert *et al.* (*BABAR* Collaboration), Phys. Rev. D **79**, 072009 (2009).
[44] B. Aubert *et al.* (*BABAR* Collaboration), Phys. Rev. D **76**, 012004 (2007).
[45] G. Punzi (2004), eConf. C030908:WELT002 (2003).
[46] H. Albrecht *et al.* (ARGUS Collaboration), Phys. Lett. B **241**, 278 (1990).
[47] B. El-Bennich, A. Furman, R. Kamiński, L. Leśniak, B. Loiseau, and B. Moussallam, Phys. Rev. D **79**, 094005 (2009).